Geol. Mag. **156** (*4*), *2019, pp. 585–604* © *Cambridge University Press 2018*
doi:10.1017/S0016756817001029

Partial melting of oceanic sediments in subduction zones and its contribution to the petrogenesis of peraluminous granites in the Chinese Altai

QUN LUO*‡, CHEN ZHANG*§¶, SHU JIANG||†, LUOFU LIU*§¶, DONGDONG LIU‡, XIANGYE KONG*‡, XIAOYU LIU§ & XINPENG WANG§

*State Key Laboratory of Petroleum Resources and Prospecting, China University of Petroleum, Beijing 102249, China
‡Unconventional Natural Gas Institute, China University of Petroleum, Beijing 102249, China
§College of Geoscience, China University of Petroleum, Beijing 102249, China
¶Basin and Reservoir Research Center, China University of Petroleum, Beijing 102249, China
||Energy & Geoscience Institute, University of Utah, Salt Lake City 84108, UT, USA

(*Received* 1 March 2017; *accepted* 27 October 2017; *first published online* 25 January 2018)

Abstract – Late Carboniferous magmatism in the Chinese Altai provides an important view of geodynamic processes active during crustal growth in the Central Asian Orogenic Belt (CAOB). In this study, five representative peraluminous granite plutons from the Chinese Altai were selected for systematic geochronological, geochemical and Sr–Nd–Hf isotopic analyses (Table 1). These granites were emplaced between 449 and 327 Ma in an active subduction zone, and have moderate to high SiO_2 (66.54–76.13 wt %), moderate $Na_2O + K_2O$ (6.27–7.66 wt %), and high Al_2O_3 contents (12.43–16.18 wt %). All granite samples in this study showed significant decoupling of the Nd and Hf isotope systems. Results show negative $\varepsilon_{Nd}(t)$ values (−3.3 to −0.9), and predominantly positive $\varepsilon_{Hf}(t)$ values (+0.24 to +8.01, $n = 57$) except for a few negative $\varepsilon_{Hf}(t)$ values (−7.44 to −0.03, n = 9), high Mg# values (28.69–53.33), high Nd/Hf ratios (4.26–43.57), and enrichment of large-ion lithophile elements (LILEs; e.g. Pb, Th, and U), suggesting that the granites were derived from the partial melting of oceanic sediments and the associated mantle wedge, with fractionation of plagioclase, K-feldspar and biotite. *In situ* zircon Hf isotopic analyses yield negative $\varepsilon_{Hf}(t)$ values from −30.6 to −13.7 for the zircon xenocrysts. The U–Pb ages and Hf isotopic ratios of these zircon xenocrysts were probably inherited from oceanic sediments. Zircon saturation temperatures suggest that these peraluminous granites were emplaced at 537–765 °C. We propose that: (1) the Nd isotopic system more faithfully reflects the source of peraluminous magmas in the Chinese Altai than the Hf isotopic system, and (2) the oceanic sediment recycling was an important process during continental growth in the CAOB.

Keywords: Central Asian Orogenic Belt, Chinese Altai, peraluminous granites, Sr–Nd–Hf isotopics, subduction

1. Introduction

The recycling of materials from a subducting slab back into the overlying crust is arguably the most important geochemical cycle on Earth (Jarrard, 1986; Anderson, 1989, 2001; Turcotte & Schubert, 2002; Conrad & Lithgow-Bertelloni, 2003; Anderson, 2006; Spandler & Pirard, 2013). The component exchange between the subducting slab and the overlying depleted mantle takes place in subduction zones. Experimental investigations (Tatsumi *et al*. 1989; Brenan *et al*. 1995; You *et al*. 1996; Kessel *et al*. 2005) and studies of active subduction arcs (McCulloch & Gamble, 1991; Pearce & Peate, 1995; Münker *et al*. 2004; Turner *et al*. 2009; Handley *et al.* 2011) have suggested that both Nd and Hf are relatively fluid-immobile elements (e.g. compared to Sr). Recent work by Chauvel *et al*. (2009) showed that altered basalts from the western Pacific are indistinguishable from unaltered Pacific MORB (mid-ocean ridge basalt) in their Hf–Nd isotopic ratios. Such results support those of previous studies (e.g. White & Patchett, 1984), which demonstrated that hydrothermal alteration has little or no effect on these ratios (cf. Sr isotopes; Staudigel *et al*. 1995) and, more importantly, provided a means of constraining the contribution of subducting sediments to island arc magmatism (Handley *et al.* 2011).

The Central Asian Orogenic Belt (CAOB), also known as the Altaids, represents the largest Phanerozoic accretionary orogenic belt in the world, situated between the Siberian, East European, Tarim and North China cratons (Fig. 1a; Jahn *et al*. 2004; Safonova *et al*. 2004; Yakubchuk, 2004; Yuan *et al*. 2007; Xiao *et al*. 2008). It is widely accepted that the CAOB developed via the episodic accretions of island arcs, ophiolites, accretionary complexes, seamounts and microcontinental blocks during the Palaeozoic (Chen & Jahn, 2004; Xiao, Kröner & Windley, 2009; Biske & Seltmann, 2010; Xiao *et al*. 2010; Su *et al*. 2011, 2012).

Previous studies have shown that more than 50 % of this growth involved the addition of mantle-derived juvenile materials (Jahn, Wu & Chen, 2000*a*; Kröner *et al*. 2014). However, numerous crustal fragments composed of ancient continental materials are also

†Author for correspondence: sjiang@egi.utah.edu

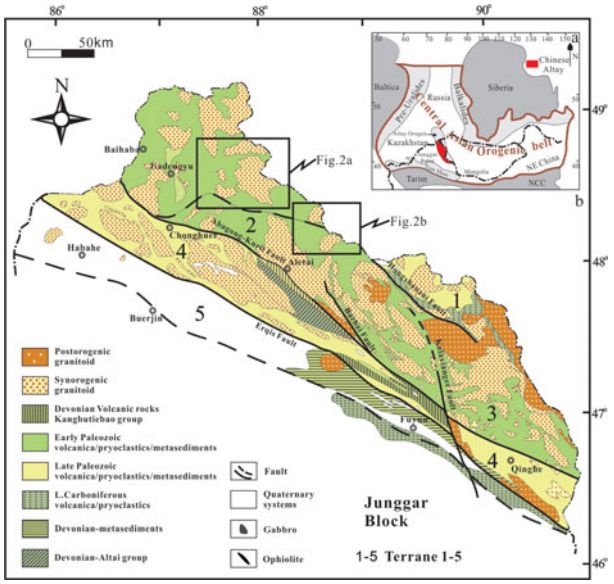

Figure 1. (Colour online) The geological sketch map of the Central Asian Orogenic Belt (CAOB) (Fig. 1a), and the Chinese Altai (Fig. 1b) (XBGMR, 1993).

believed to have played an important role in the accretionary process (Jahn, Wu & Chen, 2000*b*; Hong *et al*. 2004; Kröner *et al*. 2008). Kröner *et al*. (2014) and He *et al*. (2015) proposed that the evolution of the CAOB involved both the generation of juvenile material and the extensive reworking of older crust, and have argued that the production of juvenile crust during the amalgamation of the CAOB has been grossly overestimated.

The Chinese Altai, in the central part of the CAOB, is commonly considered to be part of Palaeozoic subduction–accretion terrane (or massif), which preserves a record of the accretion of a peri-Siberian orogenic system (Fig. 1b; Şengör *et al*., 1993; Şengör & Natal'in, 1996; Windley *et al*. 2002; Cai *et al*. 2011*a*; Long *et al*. 2012). Granites make up *c*. 40 % of exposed rocks in the Chinese Altai, and arc-related magmatism was almost continuous during the Palaeozoic, reaching a peak in the Devonian (Cai *et al*. 2011*a*,*b*, 2012, Wang *et al*. 2011; Lv *et al*. 2012). Recent studies have shown a decoupling between whole-rock Nd isotopes and zircon Hf isotopes in Early to Middle Palaeozoic granites (478–380 Ma; e.g. Yuan *et al*. 2007; Sun *et al*. 2008; Wang *et al*. 2009; Cai *et al*. 2011*a*,*b*; Yu *et al*. 2016), leading to contentious debate over the significance of this finding with respect to crustal growth of the Chinese Altai (Yu *et al*. 2016).

Based mainly on the negative $\varepsilon_{Nd}(t)$ values of some granites, Wang *et al*. (2006, 2009) proposed that the Chinese Altai is a Precambrian microcontinent derived from eastern Gondwana. In contrast, a number of other studies (Sun *et al*. 2008; Xiao *et al*. 2008; Long *et al*. 2010; Cai *et al*. 2011*b*) have argued that the Chinese Altai is an active continental margin, based on the predominantly positive zircon $\varepsilon_{Hf}(t)$ values present in both Palaeozoic granites and detrital zircons from metasedimentary rocks. In this study, we present zircon U–Pb ages, major and trace element geochemistry, and Sr, Nd and Hf isotopic compositions from representative samples of five granite plutons in the Chinese Altai, to better understand the crustal growth and tectonic evolution of the Chinese Altai.

2. Regional geology

The Altai Orogenic Belt, a major part of the CAOB in China, consists of clastic sedimentary and volcanic rocks of Ordovician to Devonian age and their metamorphosed equivalents, and extends eastward into Mongolia and westward into Kazakhstan and Russia (Fig. 1b; Windley *et al*. 2002, 2007; Xiao *et al*. 2004; Long *et al*. 2007, 2008; Sun *et al*. 2008). As the central part of the Altai Orogenic Belt, the Chinese Altai has been the subject of extensive study (Sun *et al*. 2009; Long *et al*. 2010).

The Chinese Altai can be divided into five fault-bounded terranes based on differences in stratigraphy, metamorphic grade, deformation patterns, magmatic activity and geochronology. These terranes are numbered 1–5, and are separated by the Hongshanzui, the Kalaxianger, the Abagong–Kurit and the Maerkakuli Faults (Fig. 1b; Sengör, Natal'in & Burtman, 1993; Long *et al*. 2007; Yuan *et al*. 2007; Sun *et al*. 2008; Cai *et al*. 2011*a*,*b*). Terrane 1 comprises Late Devonian to Early Carboniferous clastic sediments, limestones and sparse island-arc volcanic rocks metamorphosed to the lower greenschist facies. Terrane 2 is composed of a Middle Ordovician turbidite succession, also metamorphosed to the lower greenschist facies. Terrane 3 is the largest of the terranes, and is composed of early Palaeozoic sediments metamorphosed to a medium to high grade. Terrane 4 consists of Devonian turbiditic sandstone, pillow basalts and some siliceous volcanic rocks. Terrane 5 is composed of a fossiliferous Devonian succession, overlain by Late Carboniferous strata.

The Habahe Group is the oldest metasedimentary unit in the Chinese Altai, and is mainly composed of a thick succession (>6000 m) of slate, phyllite and schist (GCRSX, 1981; BGMRX, 1993; Windley *et al*. 2002; Long *et al*. 2007, 2008, 2010; Cai *et al*. 2012; Wang *et al*. 2014). Recent whole-rock geochemical studies, and U–Pb dating of detrital zircons from metasedimentary rocks in the Habahe Group, suggest that the original sediments were derived from parent rocks generated on an active margin in the early Palaeozoic (Long *et al*. 2007, 2010). Numerous Early to Middle Palaeozoic arc-related granites and late Palaeozoic post-collisional A-type granites are emplaced within the Habahe Group strata, providing important clues for understanding magmatism in the Chinese Altai.

3. Description of samples

Sample locations are shown in Figure 2, and hand sample photographs and photomicrographs are shown in Figure 3. The Mandalehai granites are composed

https://doi.org/10.1017/S0016756817001029 Published online by Cambridge University Press

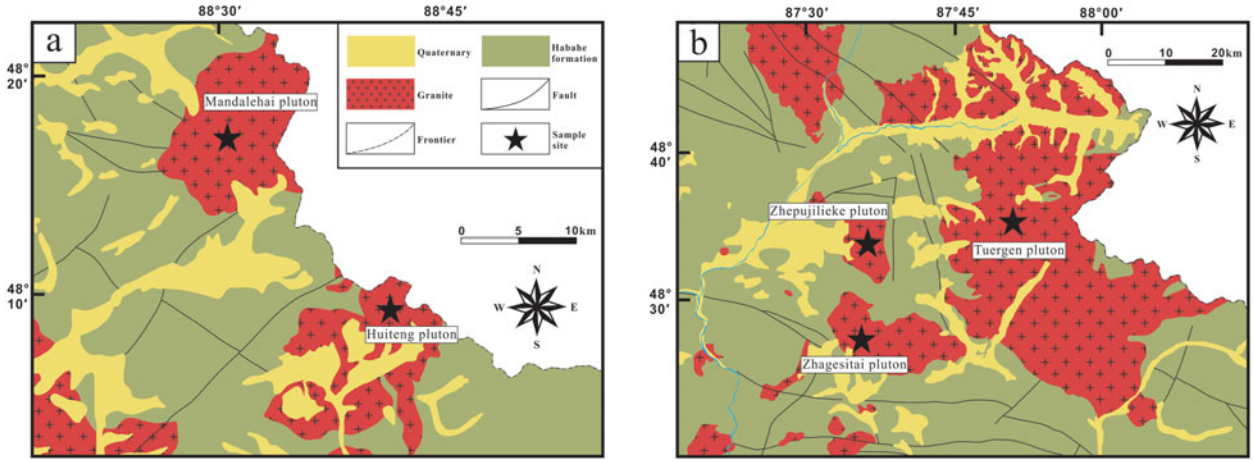

Figure 2. (Colour online) Geological sketch map of the Mandalehai and Huiteng granites (Fig. 2a), and the Zhepujileke, Tuergen and Zhagesitai granites (Fig. 2b).

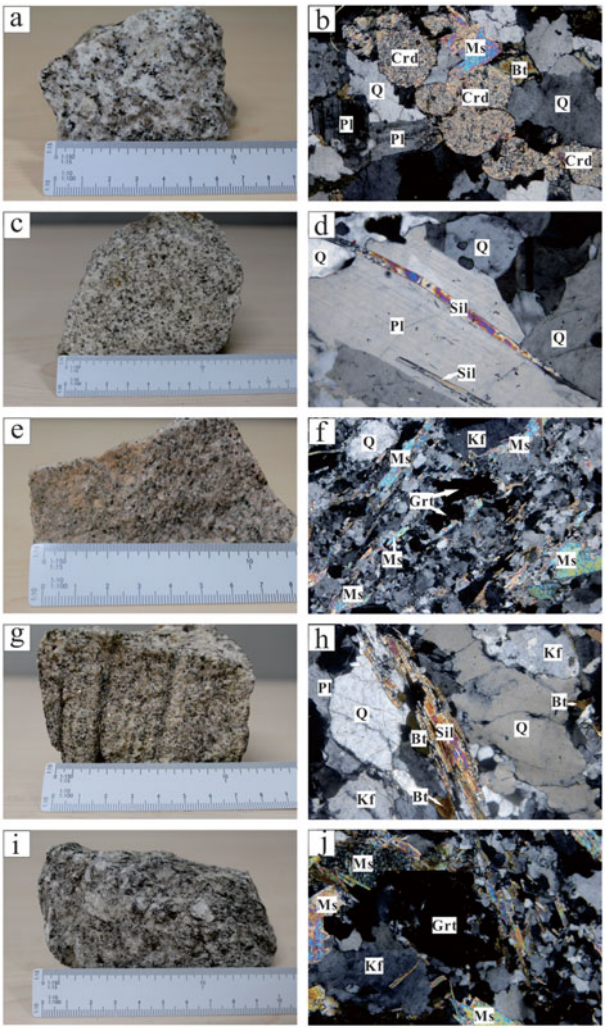

Figure 3. (Colour online) Hand specimen photos and photomicrographs (cross-polarized and magnification of 50) of granites in the Chinese Altai: (a, b) the Mandalehai granites; (c, d) the Huiteng granites; (e, f) the Tuergen granites; (g, h) the Zhagesitai granites; and (i, j) the Zhepujilieke granites.

of quartz (33–42 vol. %), plagioclase (38–43 vol. %), biotite (3–5 vol. %) and muscovite (5–10 vol. %), with accessory cordierite (Fig. 3b). The Huiteng granites consist of quartz (33–38 vol. %), K-feldspar (5–10 vol. %), plagioclase (32–37 vol. %), biotite (5–9 vol. %) and muscovite (3–5 vol. %), with sillimanite as an accessory mineral (Fig. 3d).

The Tuergen granites consist of K-feldspar (30–35 vol. %), quartz (30–40 vol. %), plagioclase (5–10 vol. %), biotite (2–5 vol. %) and muscovite (5–8 vol. %), with garnet as an accessory mineral (Fig. 3f). The Zhagestai granites are composed of quartz (25–30 vol. %), plagioclase (30–35 vol. %), K-feldspar (20–25 vol. %), biotite (2–4 vol. %) and muscovite (2–5 vol. %); accessory minerals are mainly sillimanite (Fig. 3h). The Zhepujilieke granites consist of K-feldspar (35–45 vol. %), quartz (20–25 vol. %), plagioclase (15–20 vol. %), biotite (4–6 vol. %) and muscovite (5 vol. %), with garnet as an accessory mineral (Fig. 3i).

4. Analytical methods

4.1. Major and trace element analyses

Whole-rock major and trace element compositions of the granite samples were determined at the State Key Laboratory of Ore Deposit Geochemistry, Institute of Geochemistry, Chinese Academy of Sciences (IGCAS) (Table 2). Major elements were analysed using a Leeman Prodigy inductively coupled plasma optical emission spectrometer, with high-dispersion Echelle optics. Analytical uncertainties were generally less than 1 % for most oxides, except for TiO_2 (1.5 %) and P_2O_5 (2.0 %), based on repeated analyses of US Geological Survey (USGS) standards BCR-1 and AVG-2 and the Chinese National Rock Standard GSR-3. Trace elements were analysed using an Agilent-7500a inductively coupled plasma mass spectrometer (ICP-MS). Data quality was assessed via repeated measurements of USGS reference materials BCR-1 and BHVO-1.

https://doi.org/10.1017/S0016756817001029 Published online by Cambridge University Press

The analytical precision for most trace elements was more than 95 %.

4.2. Zircon U–Pb dating

Zircon grains were isolated using standard heavy liquid and magnetic separation methods. Using a binocular microscope, we selected transparent zircon grains that were free of cracks, then fixed them in epoxy resin and polished the surface to expose the grain centres. The grain mount was then cleaned and photographed. Cathodoluminescence (CL) images were obtained using a LEO1450VP scanning electron microscope, to reveal internal structures within individual zircon grains (Fig. 4). Isotope data were collected using a laser ablation multi-collector (LA-MC) ICP-MS at the State Key Laboratory of Ore Deposit Geochemistry, IGCAS. U and Pb concentrations and isotope ratios were measured simultaneously, with an Agilent 7500a quadrupole (Q)-ICP-MS instrument. Details of the analytical procedure are described in Yuan *et al*. (2004) and Xie *et al*. (2008)

The $^{207}Pb/^{206}Pb$ and $^{206}Pb/^{238}U$ ratios were calculated using the GLITTER 4.0 program (Macquarie University, Australia) and zircon standards 91500, GJ-1 and NIST SRM 610. Age distribution histograms and concordia plots were constructed using the ISOPLOT 3.0 program, with standard Pb corrections as described by Andersen (2002) (Fig. 5). All zircon U–Pb data are reported in Table 3; all weighted mean ages are expressed with 95 % confidence intervals.

4.3. Sr–Nd isotopic analyses

The Sr and Nd isotopic compositions of the studied granite samples were measured at the Experimental Test Center, Tianjin Institute of Geology and Mineral Resources (Tianjin, China), using a VG 354 thermal ionization mass spectrometer (TIMS) in static mode. For each sample, *c*. 100–150 mg of powdered whole rock was dissolved in an HF–$HClO_4$ solution, in a screw-top Teflon beaker. The Rb, Sr, Sm and Nd concentrations were determined using the isotope dilution method, with a ^{87}Rb–^{84}Sr–^{149}Sm–^{144}Nd spiked solution (Zhang *et al*. 2001). The $^{143}Nd/^{144}Nd$ and $^{87}Sr/^{86}Sr$ ratios were normalized to $^{146}Nd/^{144}Nd = 0.7219$ and $^{86}Sr/^{88}Sr = 0.1194$, respectively. Detailed analytical methods are described in Chen & Jahn (2002). Measurements were corrected using standards NBS 607, with a $^{87}Sr/^{86}Sr$ ratio of 1.20032 ± 28 (2σ), and BCR-1, with a $^{143}Nd/^{144}Nd$ ratio of 0.512626 ± 9 (2σ). The analytical precision of the measurements was ~99 % for the $^{87}Rb/^{86}Sr$ ratio, and ~99.5 % for the $^{147}Sm/^{144}Nd$ ratio. Two-stage depleted mantle (T_{DM}) Nd model ages were calculated using a $^{143}Nd/^{144}Nd$ ratio of 0.513151 and a $^{147}Sm/^{144}Nd$ ratio of 0.21357 for the present-day depleted mantle, and an average crustal $^{147}Sm/^{144}Nd$ ratio of 0.118 (Jahn & Condie, 1995).

4.4. *In situ* zircon Hf isotopic analyses

In situ zircon Hf isotopic analyses of granite samples were conducted at Nanjing University, using a Neptune MC-ICP-MS equipped with a 193 nm laser. A laser energy of 100 mJ and a repetition rate of 10 Hz were used for all measurements; spot sizes were 32–63 μm. Raw count rates for ^{172}Yb, ^{173}Yb, ^{175}Lu, $^{176}(Hf + Yb + Lu)$, ^{177}Hf, ^{178}Hf, ^{179}Hf, ^{180}Hf and ^{182}W were collected, and corrections for the isobaric interference ^{176}Lu and ^{176}Yb on ^{176}Hf were precisely determined. ^{176}Lu was calculated using the ^{175}Lu value, while mean Yb value obtained for each spot was applied when correcting for ^{176}Yb interference; the $^{176}Yb/^{172}Yb$ ratio was assumed to be 0.5887 (Iizuka & Hirata, 2005). Measured $^{176}Hf/^{177}Hf$ and $^{176}Lu/^{177}Hf$ ratios for zircon standard 91500 were 0.282294 ± 15 (2σ, $n = 20$) and 0.00031, respectively. This $^{176}Hf/^{177}Hf$ value agrees well with the accepted $^{176}Hf/^{177}Hf$ ratios of 0.282302 ± 8 and 0.282306 ± 8 (2σ), obtained using the solution method (Goolaerts *et al*. 2004). The notations $\varepsilon_{Hf}(t)$, $f_{Lu/Hf}$, and T_{DM} are defined as in Yang *et al*. (2007), with single-stage Hf model ages interpreted from positive $\varepsilon_{Hf}(t)$ values.

5. Results

5.1. Major and trace elements

The granite samples are strongly peraluminous, with A/CNK ratios of 1.08–1.53 (molar $Al_2O_3/CaO + Na_2O + K_2O$; Fig. 6b). They are composed of 66.54–76.13 % SiO_2, 2.90–5.64 % K_2O, 1.24–3.86 % Na_2O, 1.05–4.90 % TFe_2O_3, 0.02–0.14 % MnO, 0.41–1.40 % MgO, 0.01–0.67 % TiO_2 and 0.01–0.22 % P_2O_5. Mg# [Mg/(Mg + Fe)] values of these granites range from 28.69 to 53.33 (Table 1). All of the studied samples plot within the 'subalkalic granite' field on the $(Na_2O + K_2O)$ v. SiO_2 plot (Fig. 6a).

The total rare earth element (REE) contents of the five studied granites are quite high, ranging from 92.01 to 282.05 ppm, and all samples show a characteristic enrichment in light REEs relative to heavy REEs, with $(La/Yb)_N$ ratios ranging from 4.26 to 11.75 (Fig. 7b). In addition, the granites show strong depletions in Nb and Ta, which are typical characteristics of subduction-related magmas (Fig. 7a).

5.2. Zircon U–Pb ages

Zircon grains in our granite samples are typically pale yellow, transparent, subhedral to euhedral, and 80–100 μm in size. All zircons exhibit bright cathodoluminescence, with clear concentric oscillatory zones (Fig. 4). Th concentrations of all the analysed zircons vary from 36 to 1801 ppm, while U concentrations range from 83 to 2202 ppm, yielding relatively high Th/U ratios (0.33–1.82). Zircon xenocrysts are common in the CL images; the Th/U ratios of these xenocrysts range from 0.65 to 0.93, suggesting that they are magmatic zircons.

https://doi.org/10.1017/S0016756817001029 Published online by Cambridge University Press

Figure 4. (Colour online) CL images of zircons from (a) the Mandalehai granites, (b) the Huiteng granites, (c) the Tuergen granites, (d) the Zhagesitai granites and (e) the Zhepujilieke granites.

After excluding discordant ages, LA-ICP-MS U–Pb dating of zircons yielded ages of 408.2 ± 4.8 Ma for the Mandalehai granites, 327.7 ± 5.6 Ma for the Huiteng granites, 400.1 ± 3.5 Ma for the Tuergen granites, 449.8 ± 4.5 Ma for the Zhagesitai granites and 433 ± 5.9 Ma for the Zhepujilieke granites (Fig. 5; Table 3). The U–Pb ages of the xenocrysts yielded a wider range of ages, from 1294 to 913 Ma, indicating zircon crystallization in the source magma (Table 3).

5.3. Sr–Nd isotopic compositions

All samples yielded high initial $^{87}Sr/^{86}Sr$ ratios (0.714998–0.743426), and negative $\varepsilon_{Nd}(t)$ values (−3.3

https://doi.org/10.1017/S0016756817001029 Published online by Cambridge University Press

Table 1. The major chemical compositions (in wt %) and calculated parameters of the five studied granites

Sample number	MDLH-01	MDLH-02	MDLH-03	MDLH-04	HT-01	HT-02	HT-03	HT-04
SiO_2	75.63	77.47	74.76	74.15	72.71	72.97	73.29	70.52
Al_2O_3	14.94	14.96	15.95	16.16	13.66	13.63	14.32	14.91
TiO_2	0.15	0.10	0.13	0.16	0.25	0.25	0.23	0.32
TFe_2O_3	1.45	1.31	1.38	1.51	2.50	2.08	2.40	3.37
MgO	0.64	0.53	0.69	0.50	0.69	0.63	0.74	0.61
CaO	1.32	1.25	1.45	1.44	1.17	1.31	1.43	1.33
Na_2O	1.25	1.24	1.26	1.27	3.11	3.15	3.02	3.33
K_2O	5.39	5.32	5.24	5.64	4.20	4.26	3.47	4.24
MnO	0.02	0.02	0.03	0.03	0.08	0.07	0.09	0.09
P_2O_5	0.01	0.01	0.01	0.01	0.12	0.11	0.09	0.11
LOI	1.11	0.73	0.14	0.76	1.14	0.78	1.18	0.81
Total	99.76	99.89	99.95	100.18	99.68	99.30	99.87	99.59
A/CNK	1.45	1.48	1.53	1.49	1.16	1.12	1.26	1.19
A/NK	1.89	1.91	2.06	1.97	1.41	1.39	1.64	1.48
$Mg^{\#}$	49.52	47.34	52.63	42.39	38.02	40.23	40.66	28.69
$K_2O + Na_2O$	6.64	6.56	6.5	6.91	7.31	7.41	6.49	7.57
Na_2O/K_2O	0.23	0.23	0.24	0.23	0.74	0.74	0.87	0.79
Sample number	TEG-01	TEG-02	TEG-03	TEG-04	ZGST-01	ZGST-02	ZGST-03	ZGST-04
SiO_2	72.97	73.26	73.04	71.84	68.70	68.60	69.75	66.54
Al_2O_3	12.43	12.68	13.02	13.91	14.39	14.84	15.85	16.18
TiO_2	0.37	0.45	0.38	0.53	0.57	0.58	0.56	0.67
TFe_2O_3	4.09	4.33	3.94	4.90	4.11	4.20	3.96	4.75
MgO	1.00	1.03	1.05	1.01	1.35	1.40	1.40	1.38
CaO	0.78	0.97	0.81	0.98	2.09	2.46	2.85	2.50
Na_2O	3.11	3.64	3.02	3.86	3.15	3.18	3.06	3.37
K_2O	4.29	3.06	3.75	2.90	3.94	3.69	3.21	3.60
MnO	0.09	0.12	0.10	0.14	0.10	0.09	0.11	0.11
P_2O_5	0.06	0.04	0.06	0.04	0.18	0.18	0.22	0.19
LOI	0.54	0.63	0.55	0.67	1.20	1.38	1.24	1.38
Total	99.81	100.28	99.83	100.31	99.86	100.68	100.05	100.98
A/CNK	1.11	1.14	1.24	1.23	1.08	1.08	1.16	1.16
A/NK	1.27	1.36	1.44	1.46	1.52	1.61	1.86	1.71
$Mg^{\#}$	35.21	34.58	37.19	31.42	42.19	42.55	44.00	39.23
$K_2O + Na_2O$	7.40	6.70	6.77	6.76	7.09	6.87	6.27	6.97
Na_2O/K_2O	0.72	1.19	0.81	1.33	0.80	0.86	0.95	0.94
Sample number	ZPJLK-01	ZPJLK-02	ZPJLK-03	ZPJLK-04				
SiO_2	76.13	75.30	75.03	72.41				
Al_2O_3	14.60	14.54	15.33	15.74				
TiO_2	<0.01	<0.01	<0.01	0.01				
TFe_2O_3	1.05	1.25	1.20	1.21				
MgO	0.54	0.43	0.59	0.41				
CaO	1.20	1.39	1.42	1.19				
Na_2O	3.37	3.30	3.59	3.61				
K_2O	4.13	4.32	3.99	4.05				
MnO	0.02	0.03	0.04	0.03				
P_2O_5	<0.01	<0.01	0.01	<0.01				
LOI	0.05	0.47	0.48	1.53				
Total	101.14	100.63	101.03	101.23				
A/CNK	1.20	1.15	1.20	1.26				
A/NK	1.46	1.44	1.50	1.52				
$Mg^{\#}$	53.33	43.32	52.21	42.95				
$K_2O + Na_2O$	7.50	7.62	7.58	7.66				
Na_2O/K_2O	0.82	0.76	0.90	0.89				

Note: A = Al_2O_3, C = CaO, N = Na_2O, K = K_2O (all in molar proportion), Mg* = 100 $Mg^{2+}/(Mg^{2+} + Fe^{2+})$.

to −0.9; Fig. 8a; Table 4). The uniformly negative $\varepsilon_{Nd}(t)$ values and wide range of initial $^{87}Sr/^{86}Sr$ ratios in the samples can be interpreted in the context of a two-component mixing model (Han *et al.* 1997). The depleted mantle Nd model (T_{DM2}) yields quite old ages for the studied granites, ranging from 1120 to 1290 Ma.

5.4. Zircon Hf isotopic compositions

The measured Hf isotopic compositions of the five studied granite samples are shown in Figure 8b; analytical results are listed in Table 5. The $\varepsilon_{Hf}(t)$ values were calculated using the U–Pb ages of the zircons, and range from −7.4 to +8.0. The depleted mantle Hf model ages (T_{DM2}) of the granite samples range from 948 to 1801 Ma. However, the $\varepsilon_{Hf}(t)$ values and depleted mantle Nd model ages (T_{DM2}) of the zircon xenocrysts are distinct; $\varepsilon_{Hf}(t)$ values range from −30.6 to −13.7, and T_{DM2} ages range from 2190 to 3243 Ma.

6. Discussion

6.1. Peraluminous granitic magmatism in the Chinese Altai

The zircon U–Pb dating results for the five peraluminous granites in this study reveal that these intrusions were emplaced between 449 and 327 Ma.

https://doi.org/10.1017/S0016756817001029 Published online by Cambridge University Press

Table 2. Trace element compositions (in ppm) of the five studied granites

Sample number	MDLH-01	MDLH-02	MDLH-03	MDLH-04	HT-01	HT-02	HT-03	HT-04
Li	59.06	48.52	60.52	57.04	70.72	68.40	71.98	77.93
Be	3.01	2.65	3.35	2.48	3.25	2.34	3.61	2.17
Co	0.65	0.65	1.46	1.55	3.70	4.10	4.84	5.26
Ga	27.40	24.95	34.04	27.23	14.75	13.75	20.59	15.93
Ge	0.17	0.22	0.17	0.31	0.19	0.22	0.19	0.31
Rb	90.00	73.00	86.00	69.00	94.00	82.00	104.00	107.00
Sr	200.60	240.40	230.61	260.10	73.10	86.00	76.64	86.47
Y	33.66	34.87	38.45	35.30	38.50	40.70	42.10	36.40
Zr	87.55	75.05	77.70	67.20	23.40	23.40	27.86	13.66
Nb	13.33	8.80	12.58	11.93	9.70	8.30	9.27	11.38
Cs	3.59	3.31	4.95	2.82	10.45	9.75	12.32	9.28
Ba	640.00	640.00	682.00	629.00	270.00	350.00	294.00	345.60
La	29.29	51.50	32.76	58.15	29.00	29.40	32.53	33.20
Ce	48.77	95.72	54.17	114.68	63.10	64.00	70.19	76.69
Pr	6.53	11.95	7.26	13.38	7.50	7.72	8.4	8.65
Nd	26.46	48.40	29.62	54.32	30.90	31.60	34.67	35.47
Sm	5.60	10.45	6.34	11.84	7.18	7.32	8.13	8.29
Eu	1.40	2.14	1.57	2.40	1.36	1.49	1.53	1.67
Gd	5.17	8.78	5.80	9.92	6.81	6.93	7.64	7.83
Tb	0.76	1.06	0.86	1.20	1.07	1.06	1.21	1.20
Dy	5.06	5.90	5.73	6.72	6.57	6.45	7.44	7.35
Ho	1.09	1.09	1.22	1.22	1.28	1.24	1.44	1.39
Er	3.59	3.23	3.99	3.59	3.75	3.66	4.17	4.07
Tm	0.55	0.45	0.61	0.50	0.54	0.51	0.60	0.57
Yb	3.94	3.18	4.18	3.55	3.40	3.25	3.78	3.63
Lu	0.65	0.51	0.74	0.58	0.48	0.45	0.54	0.51
Hf	6.24	4.10	5.95	4.67	1.20	1.20	1.26	1.58
Ta	1.21	0.55	1.27	0.45	0.96	0.75	1.02	0.64
Pb	101.08	112.97	271.97	217.16	22.30	24.80	24.97	27.01
Th	20.84	14.10	18.96	17.69	7.28	8.81	5.98	11.71
U	3.63	2.40	3.16	2.19	2.90	3.00	2.47	2.91
Sample number	TEG-01	TEG-02	TEG-03	TEG-04	ZGST-01	ZGST-02	ZGST-03	ZGST-04
Li	36.00	41.20	37.98	49.37	52.00	54.00	53.66	62.81
Be	1.00	1.37	1.11	1.21	1.94	1.93	2.16	1.77
Co	4.60	4.00	5.82	5.15	8.30	8.80	9.86	10.24
Ga	15.25	16.15	21.12	18.36	16.15	16.95	22.08	19.17
Ge	0.15	0.16	0.15	0.23	0.23	0.24	0.23	0.33
Rb	112.00	91.00	93.00	86.00	112.00	118.00	90.00	93.00
Sr	126.50	127.50	130.57	127.14	181.50	158.50	186.12	157.52
Y	37.90	40.60	33.64	35.20	35.90	34.10	40.77	34.66
Zr	5.20	3.40	8.93	12.65	20.10	20.50	24.42	11.02
Nb	11.30	15.90	10.74	13.70	11.20	11.40	10.65	14.79
Cs	5.39	5.35	6.89	4.87	6.42	7.35	7.99	6.87
Ba	530.00	370.00	567.00	365.00	420.00	460.00	451.00	453.00
La	23.80	30.30	26.70	34.21	15.10	24.50	16.94	27.66
Ce	52.20	64.40	58.06	77.17	37.80	58.20	42.05	69.74
Pr	6.20	7.35	6.90	8.23	4.10	6.42	4.50	7.19
Nd	25.80	30.50	28.94	34.23	15.80	24.90	17.73	27.95
Sm	5.75	6.67	6.51	7.56	3.73	5.90	4.22	6.68
Eu	1.47	1.62	1.65	1.82	0.72	0.82	0.81	0.92
Gd	5.85	6.54	6.56	7.39	3.79	5.56	4.25	6.28
Tb	0.90	0.99	1.02	1.12	0.64	0.89	0.72	1.01
Dy	5.55	5.98	6.28	6.82	3.96	5.19	4.48	5.92
Ho	1.13	1.21	1.27	1.36	0.77	1.00	0.86	1.12
Er	3.44	3.55	3.83	3.94	2.34	2.91	2.60	3.23
Tm	0.46	0.50	0.51	0.56	0.36	0.44	0.40	0.49
Yb	2.96	3.09	3.29	3.45	2.54	3.04	2.82	3.40
Lu	0.46	0.48	0.52	0.54	0.36	0.44	0.41	0.50
Hf	0.69	0.70	0.71	0.82	0.90	0.90	0.96	1.26
Ta	0.59	0.77	0.65	0.82	0.90	0.96	0.96	0.84
Pb	24.40	17.70	27.05	19.77	35.20	23.10	37.74	25.28
Th	13.90	14.75	12.33	18.42	12.35	11.70	10.84	14.97
U	2.30	2.30	1.88	2.08	1.40	1.40	0.99	1.00
Sample number	ZPJLK-01	ZPJLK-02	ZPJLK-03	ZPJLK-04				
Li	96.00	99.70	100.50	106.81				
Be	4.32	4.32	4.81	4.13				
Co	0.20	0.30	1.25	1.02				
Ga	41.60	40.30	48.21	43.72				
Ge	0.14	0.17	0.19	0.19				
Rb	90.00	110.00	88.00	87.00				
Sr	210.00	240.00	270.00	230.00				
Y	28.20	24.30	20.30	26.70				
Zr	48.60	54.70	61.45	35.68				

https://doi.org/10.1017/S0016756817001029 Published online by Cambridge University Press

Table 2. Continued

Sample number	ZPJLK-01	ZPJLK-02	ZPJLK-03	ZPJLK-04
Nb	11.70	11.30	11.20	9.90
Cs	11.60	12.10	14.23	11.02
Ba	550.50	680.40	945.00	648.60
La	27.30	25.10	30.63	28.34
Ce	56.50	54.80	62.85	65.67
Pr	6.50	6.34	7.20	7.10
Nd	25.30	25.50	28.38	28.62
Sm	5.11	5.66	5.79	6.41
Eu	1.05	1.06	1.18	1.19
Gd	4.65	5.59	5.22	6.32
Tb	0.69	0.92	0.78	1.04
Dy	4.18	5.90	4.73	6.71
Ho	0.80	1.17	0.90	1.31
Er	2.28	3.40	2.54	3.78
Tm	0.32	0.46	0.36	0.51
Yb	2.04	2.90	2.27	3.20
Lu	0.31	0.39	0.35	0.44
Hf	5.80	5.50	5.32	6.41
Ta	0.79	0.82	0.69	0.99
Pb	77.70	111.50	113.08	81.17
Th	20.40	24.00	22.12	24.69
U	1.50	3.40	3.06	1.00

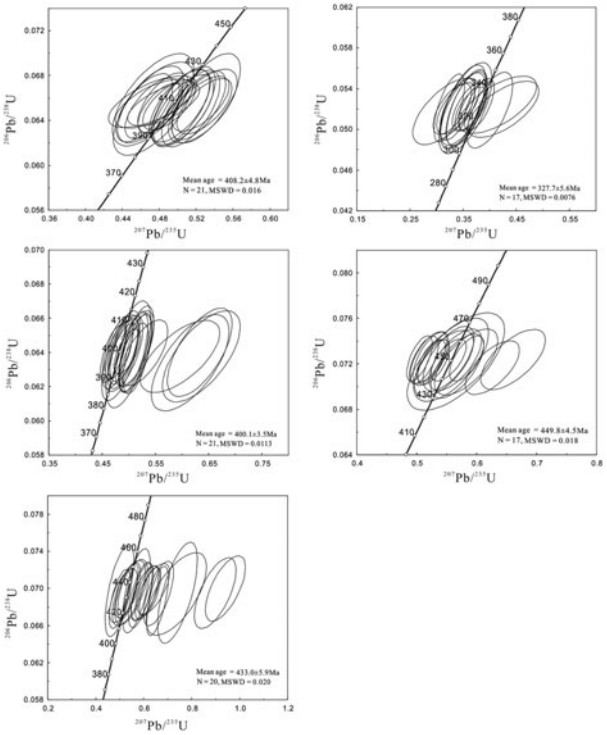

Figure 5. U–Pb concordia diagrams for zircons from (a) the Mandalehai granites, (b) the Huiteng granites, (c) the Tuergen granites, (d) the Zhagesitai granites and (e) the Zhepujilieke granites.

Synchronous felsic volcanism is also apparent in the form of peraluminous rhyolites in the study area, which have yielded U–Pb zircon ages of 406 to 412 Ma (Chai *et al*. 2009; Long *et al*. 2010; Wang *et al*. 2011; Cai *et al*. 2012). Other peraluminous and S-type granites have also been dated, and given comparable zircon U–Pb ages (507 Ma to 392 Ma; Tong *et al*. 2007; Cai *et al*. 2011*a*; Zhang *et al*. 2016). Peraluminous granitic magmatism appears to have occurred over a

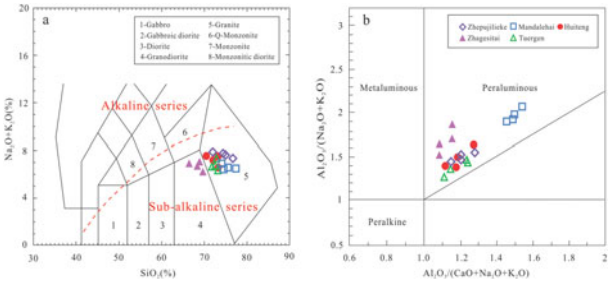

Figure 6. (Colour online) Chemical classification diagrams for the studied granite samples. (a) Total alkali ($K_2O + Na_2O$) v. SiO_2 diagram (compositional fields from Middlemost, 1994); (b) A/NK v. A/CNK diagram (Maniar and Piccoli, 1989).

long period in the Chinese Altai, spanning from 507 to 327 Ma.

All of the studied peraluminous granites plot in the 'VAG + syn-COLG' field on the Nb v. Y and 'VAG' field Rb v. (Y + Nb) plots (Fig. 9a, b), and in the 'Classical island arc' and 'Normal arc magmas' field on the $(La/Yb)_N$ v. $(Yb)_N$ and Sr/Y v. Y plots (Fig. 10a, b), indicating that these granites are most likely petrogenetically associated with arc magmatism. These results agree well with the subduction tectonic setting inferred for the Chinese Altay during the Palaeozoic (Yuan *et al*. 2007; Sun *et al*. 2008; Cai *et al*. 2011*a*,*b*; Xiao *et al*. 2011; Xiao & Santosh, 2014; Zhang *et al*. 2016).

6.2. Petrogenesis

6.2.1. Magma sources

Previous studies have suggested that peraluminous granites are mainly generated by the partial melting of metasedimentary rocks such as metapelite and metagreywacke, with the possible addition of

https://doi.org/10.1017/S0016756817001029 Published online by Cambridge University Press

Table 3. U-–Pb dating results of the studied five granites

Sample	Th(ppm)	U(ppm)	Th/U	Ratio						Age (Ma)			
				$^{207}Pb/^{206}Pb$	1σ	$^{207}Pb/^{235}U$	1σ	$^{206}Pb/^{238}U$	1σ	$^{207}Pb/^{235}U$	1σ	$^{206}Pb/^{238}U$	1σ
Mandalehai													
Mandalehai-01	307.86	446.27	0.69	0.055443	0.002292	0.502391	0.021888	0.065315	0.002127	413.3	4.8	407.9	2.9
Mandalehai-02	303.95	321.36	0.95	0.052020	0.003049	0.473447	0.029098	0.065847	0.002721	393.6	2.1	411.1	2.5
Mandalehai-03	4087.71	4468.47	0.91	0.285157	0.014686	2.122275	0.139530	0.252815	0.009744	1156.1	25.3	1048.6	19.2
Mandalehai-04	780.23	600.13	1.30	0.058034	0.002080	0.530938	0.024387	0.065993	0.002624	432.4	3.2	412.0	2.9
Mandalehai-05	1200.15	784.03	1.53	0.055978	0.001850	0.506456	0.021628	0.064961	0.002070	416.1	4.6	405.7	2.5
Mandalehai-06	476.29	542.87	0.88	0.051461	0.002231	0.464114	0.020339	0.065136	0.002010	387.1	4.1	406.8	2.2
Mandalehai-07	3955.4	4341.7	0.91	0.277777	0.013001	2.056184	0.130423	0.252441	0.008555	1134.4	33.3	1095.7	15.4
Mandalehai-08	129.16	295.32	0.44	0.051919	0.003612	0.472828	0.031546	0.065679	0.001529	393.1	2.8	410.1	6.3
Mandalehai-09	1801.08	989.87	1.82	0.058133	0.002331	0.527371	0.024709	0.065292	0.002171	430.1	3.4	407.7	3.1
Mandalehai-10	289.77	438.68	0.66	0.052797	0.002033	0.484207	0.018178	0.065575	0.001765	401.0	2.4	409.4	4.7
Mandalehai-11	292.32	310.28	0.94	0.052401	0.002929	0.474075	0.028883	0.065057	0.002744	394.0	2.9	406.3	3.6
Mandalehai-12	774.02	594.70	1.30	0.056774	0.001911	0.514399	0.020679	0.065085	0.002255	421.4	3.9	406.5	3.7
Mandalehai-13	1254.15	783.89	1.60	0.055735	0.001877	0.506820	0.022731	0.065241	0.002360	416.3	5.3	407.4	4.3
Mandalehai-14	484.35	543.65	0.89	0.052129	0.001958	0.472630	0.019508	0.065073	0.001778	393.0	3.5	406.4	3.8
Mandalehai-15	127.31	289.52	0.44	0.051966	0.003032	0.474247	0.027794	0.065507	0.001444	394.1	9.1	409.0	8.7
Mandalehai-16	1713.3	971.02	1.76	0.057517	0.002069	0.524883	0.020571	0.065496	0.001613	428.4	3.7	409.0	9.8
Mandalehai-17	258.76	429.87	0.60	0.052929	0.001901	0.481100	0.016115	0.065134	0.001468	398.8	5.0	406.8	5.9
Mandalehai-18	263.28	301.90	0.87	0.051721	0.002434	0.470559	0.023754	0.065447	0.002260	391.6	56.4	408.7	3.7
Mandalehai-19	749.63	576.40	1.30	0.057512	0.001742	0.522585	0.019338	0.065343	0.002020	426.9	2.9	408.0	2.2
Mandalehai-20	1296.23	776.86	1.67	0.055806	0.001920	0.502955	0.020994	0.065177	0.002250	413.7	4.2	407.0	3.6
Mandalehai-21	778.33	568.16	1.37	0.053923	0.001880	0.490799	0.018946	0.065386	0.001466	405.5	2.9	408.3	5.9
Mandalehai-22	121.17	278.47	0.44	0.052970	0.002634	0.484691	0.025778	0.065456	0.001269	401.3	7.6	408.7	7.7
Mandalehai-23	1644.26	944.15	1.74	0.058190	0.001798	0.528986	0.019708	0.065286	0.001632	431.1	3.1	407.7	4.9
Huiteng													
Huiteng-01	85.48	142.54	0.60	0.046431	0.003476	0.329755	0.023801	0.052033	0.001649	289.4	6.2	327.0	5.1
Huiteng-02	98.56	258.01	0.38	0.047999	0.002994	0.338929	0.021917	0.051962	0.001997	296.4	4.6	326.6	2.2
Huiteng-03	258.41	656.69	0.39	0.050078	0.003183	0.356370	0.025465	0.052069	0.002399	309.5	4.1	327.2	4.7
Huiteng-04	1248.23	1902.8	0.66	0.274942	0.011836	2.739708	0.174094	0.270474	0.005602	1339.3	25.9	1274.6	22.3
Huiteng-05	50.83	96.17	0.53	0.059777	0.005943	0.425522	0.044432	0.051970	0.001832	360.0	1.7	331.6	3.2
Huiteng-06	1258.57	1940.46	0.65	0.269821	0.020242	2.653696	0.292720	0.268579	0.003380	1315.7	41.5	1293.5	17.6
Huiteng-07	230.69	529.65	0.44	0.050000	0.002325	0.363570	0.019559	0.052039	0.001412	314.9	4.6	327.0	4.7
Huiteng-08	106.53	178.20	0.60	0.051374	0.002647	0.368728	0.018297	0.052196	0.001531	318.7	3.6	328.0	4.4
Huiteng-09	68.92	120.43	0.57	0.049772	0.004396	0.354117	0.032904	0.052097	0.002944	307.8	4.7	327.4	3.0
Huiteng-10	105.81	272.98	0.39	0.050230	0.003603	0.356963	0.025540	0.052097	0.002492	309.9	4.1	327.4	5.3
Huiteng-11	35.74	83.67	0.43	0.047508	0.007896	0.317731	0.041513	0.051779	0.002159	280.2	4.0	325.4	3.2
Huiteng-12	2530.79	3631.72	0.70	0.184585	0.008602	1.811861	0.148637	0.270016	0.008478	1049.75	23.2	936.2	21.0
Huiteng-13	238.49	524.21	0.45	0.048272	0.003364	0.349980	0.027775	0.052016	0.002357	304.7	5.9	326.9	4.4
Huiteng-14	110.77	173.79	0.64	0.056073	0.004389	0.399990	0.028507	0.051895	0.002470	341.6	4.7	326.1	5.1
Huiteng-15	86.71	143.47	0.60	0.047120	0.003385	0.336236	0.023927	0.052071	0.001673	294.3	6.2	327.2	5.2
Huiteng-16	98.47	259.86	0.38	0.046131	0.002914	0.323662	0.018975	0.052106	0.002186	284.7	4.6	327.4	3.4
Huiteng-17	258.39	658.48	0.39	0.049123	0.003497	0.349658	0.028236	0.052202	0.002709	304.5	6.2	328.0	6.6
Huiteng-18	50.79	96.01	0.53	0.058284	0.006512	0.415533	0.048180	0.052420	0.001857	352.9	4.6	329.4	7.4
Huiteng-19	232.10	527.48	0.44	0.049598	0.002578	0.361765	0.021525	0.052223	0.001572	313.5	6.1	328.2	6.6
Huiteng-20	107.64	178.57	0.60	0.052663	0.002676	0.379990	0.018722	0.052448	0.001680	327.0	3.8	329.5	5.3

Table 3. Continued

Sample	Th(ppm)	U(ppm)	Th/U	Ratio						Age (Ma)			
				$^{207}Pb/^{206}Pb$	1σ	$^{207}Pb/^{235}U$	1σ	$^{206}Pb/^{238}U$	1σ	$^{207}Pb/^{235}U$	1σ	$^{206}Pb/^{238}U$	1σ
Tuergen													
Tuergen-01	158.83	307.84	0.52	0.056541	0.002650	0.499624	0.027956	0.063886	0.002063	411.4	5.9	399.2	5.5
Tuergen-02	506.62	587.98	0.86	0.058509	0.002758	0.512226	0.019899	0.063971	0.001479	419.9	3.4	399.7	4.0
Tuergen-03	231.86	311.26	0.74	0.057836	0.002899	0.510912	0.024166	0.064235	0.001453	419.1	6.2	401.3	5.8
Tuergen-04	518.08	595.40	0.87	0.055368	0.002456	0.490971	0.023888	0.063949	0.001470	405.6	5.3	399.6	5.9
Tuergen-05	1246.82	1836.65	0.68	0.276123	0.014386	2.733563	0.208052	0.269914	0.006865	1337.6	26.6	1244.3	21.1
Tuergen-06	379.42	478.18	0.79	0.054221	0.001886	0.481738	0.017765	0.064155	0.001129	399.3	2.2	400.8	3.8
Tuergen-07	646.71	646.85	1.00	0.057884	0.001971	0.514704	0.020925	0.064193	0.001680	421.6	4.0	401.1	4.2
Tuergen-08	488.09	564.12	0.87	0.071843	0.006727	0.615274	0.048005	0.063407	0.001857	486.9	5.2	396.3	6.3
Tuergen-09	155.95	304.99	0.51	0.055035	0.002304	0.484518	0.023201	0.063699	0.001647	401.2	5.9	398.1	5.0
Tuergen-10	485.84	568.15	0.86	0.058048	0.002362	0.508998	0.018468	0.063850	0.001227	417.8	7.4	399.0	7.4
Tuergen-11	219.19	300.70	0.73	0.059766	0.003006	0.529260	0.029098	0.063991	0.001270	431.3	4.3	399.9	2.7
Tuergen-12	543.68	599.56	0.91	0.054243	0.002108	0.479370	0.019304	0.064005	0.001409	397.6	3.3	399.9	6.5
Tuergen-13	3440.14	4428.18	0.78	0.201205	0.007283	1.952109	0.110338	0.270028	0.009949	1099.17	38.0	1017.3	17.8
Tuergen-14	362.74	464.04	0.78	0.055325	0.001726	0.491697	0.017430	0.064149	0.001218	406.1	5.9	400.8	5.4
Tuergen-15	637.81	644.88	0.99	0.057571	0.001910	0.508637	0.018113	0.064039	0.001570	417.5	2.2	400.1	4.5
Tuergen-16	452.74	544.74	0.83	0.075071	0.007118	0.636417	0.048055	0.063770	0.001754	500.1	9.8	398.5	10.6
Tuergen-17	152.23	300.83	0.51	0.055443	0.002112	0.490520	0.020280	0.064160	0.001497	405.3	3.8	400.9	4.1
Tuergen-18	450.54	538.68	0.84	0.056190	0.001885	0.496828	0.016199	0.064048	0.000851	409.6	7.0	400.2	5.2
Tuergen-19	210.20	292.16	0.72	0.066710	0.004525	0.596408	0.048962	0.063777	0.001384	475.0	4.2	398.6	3.4
Tuergen-20	561.70	601.71	0.93	0.055373	0.001868	0.489861	0.017941	0.063929	0.001183	404.8	3.2	399.5	5.2
Tuergen-21	359.37	459.82	0.78	0.053201	0.001622	0.471598	0.016269	0.063937	0.001119	392.3	6.2	399.5	4.8
Tuergen-22	638.22	643.83	0.99	0.058997	0.002212	0.516486	0.017990	0.063948	0.001555	422.8	2.0	399.6	3.4
Tuergen-23	431.84	532.57	0.81	0.074758	0.006130	0.633179	0.040035	0.064005	0.001706	498.1	4.9	399.9	3.3
Zhagesitai													
Zhagesitai-01	185.33	561.23	0.33	0.071860	0.003856	0.657065	0.029999	0.068647	0.002465	512.8	6.4	428.0	4.9
Zhagesitai-02	313.26	387.52	0.81	0.061482	0.002326	0.594361	0.030401	0.069602	0.002055	473.6	6.4	433.8	3.4
Zhagesitai-03	204.81	233.73	0.88	0.064790	0.002614	0.626097	0.029864	0.069668	0.001748	493.7	4.7	434.2	5.5
Zhagesitai-04	81.31	160.97	0.51	0.055081	0.003124	0.533473	0.035049	0.069785	0.001976	434.1	3.2	434.9	3.9
Zhagesitai-05	354.37	417.62	0.85	0.096020	0.004013	0.939925	0.054930	0.069986	0.002317	672.8	5.8	436.1	4.0
Zhagesitai-06	116.14	125.74	0.92	0.063214	0.003921	0.606413	0.039720	0.069549	0.001925	481.3	5.1	433.4	4.6
Zhagesitai-07	252.76	336.65	0.75	0.055566	0.002721	0.533309	0.028324	0.069703	0.002005	434.0	8.8	434.4	2.1
Zhagesitai-08	162.45	445.00	0.37	0.066239	0.004229	0.640162	0.044715	0.069932	0.001816	502.4	7.7	435.7	2.9
Zhagesitai-09	355.95	399.68	0.89	0.059265	0.003011	0.569108	0.037933	0.069749	0.003003	457.4	4.6	434.6	8.1
Zhagesitai-10	184.37	209.74	0.88	0.056341	0.003560	0.547391	0.044630	0.069595	0.002315	443.3	9.3	433.7	4.0
Zhagesitai-11	82.20	160.91	0.51	0.056115	0.004145	0.537298	0.045373	0.069523	0.002318	436.6	5.0	433.3	4.0
Zhagesitai-12	96.79	120.26	0.80	0.078731	0.005596	0.740290	0.054303	0.069542	0.003590	562.6	3.7	433.4	2.6
Zhagesitai-13	294.60	367.34	0.80	0.052170	0.003432	0.498935	0.038884	0.069783	0.003263	411.0	6.3	434.8	4.7
Zhagesitai-14	164.04	479.23	0.34	0.078839	0.009217	0.735785	0.082633	0.069415	0.002931	559.9	4.4	432.6	6.7
Zhagesitai-15	336.99	404.13	0.83	0.060870	0.002343	0.585567	0.032706	0.069315	0.002324	468.0	3.9	432.0	4.0
Zhagesitai-16	210.42	238.32	0.88	0.063790	0.002901	0.613310	0.032258	0.069550	0.001922	485.6	4.3	433.4	5.6
Zhagesitai-17	82.44	163.24	0.51	0.053872	0.003504	0.515773	0.037823	0.069231	0.001917	422.3	5.3	431.5	3.6
Zhagesitai-18	384.71	446.15	0.86	0.092572	0.004295	0.896782	0.057619	0.069511	0.002520	650.0	5.9	433.2	5.2
Zhagesitai-19	98.36	117.78	0.84	0.070405	0.004628	0.661835	0.041192	0.069444	0.002297	515.7	5.2	432.8	3.8
Zhagesitai-20	273.61	355.04	0.77	0.052716	0.002802	0.499498	0.029304	0.068899	0.002098	411.4	9.8	429.5	2.7

Table 3. Continued

Sample	Th(ppm)	U(ppm)	Th/U	Ratio						Age (Ma)			
				$^{207}Pb/^{206}Pb$	1σ	$^{207}Pb/^{235}U$	1σ	$^{206}Pb/^{238}U$	1σ	$^{207}Pb/^{235}U$	1σ	$^{206}Pb/^{238}U$	1σ
Zhepujilieke													
Zhepujilieke-01	321.99	615.57	0.52	0.066280	0.003486	0.660597	0.035700	0.072370	0.001748	515.0	5.8	450.4	5.5
Zhepujilieke-02	394.44	681.62	0.58	0.055781	0.002119	0.553207	0.019510	0.072342	0.001231	447.1	2.8	445.3	4.4
Zhepujilieke-03	3111.4	3999.8	0.78	0.194340	0.006825	1.781895	0.092095	0.266209	0.012415	1038.9	28.6	913.3	14.6
Zhepujilieke-04	242.48	511.45	0.47	0.057022	0.005029	0.557541	0.041207	0.072367	0.002405	449.9	6.9	457.4	4.5
Zhepujilieke-05	1085.78	1287.45	0.84	0.051674	0.001699	0.511704	0.016079	0.072347	0.001378	419.6	5.8	450.3	4.3
Zhepujilieke-06	583.92	1713.93	0.34	0.058176	0.002634	0.582275	0.034940	0.072164	0.001920	465.9	2.4	449.2	2.5
Zhepujilieke-07	1486.77	2193.17	0.68	0.053297	0.001607	0.527877	0.017438	0.072158	0.001310	430.4	5.6	449.1	5.9
Zhepujilieke-08	331.76	648.08	0.51	0.063297	0.002970	0.625990	0.029778	0.071655	0.001560	493.6	8.6	446.1	4.4
Zhepujilieke-09	445.05	627.99	0.71	0.058228	0.001727	0.583231	0.018962	0.072463	0.001310	466.5	2.2	451.0	5.9
Zhepujilieke-10	240.95	511.20	0.47	0.055726	0.004013	0.545389	0.032539	0.072055	0.001913	442.0	4.4	448.5	3.5
Zhepujilieke-11	1006.84	1228.32	0.82	0.050735	0.001509	0.504658	0.014104	0.072478	0.001307	414.9	3.5	451.1	2.9
Zhepujilieke-12	564.63	1549.99	0.36	0.056938	0.002221	0.567883	0.029232	0.071818	0.001865	456.6	5.9	447.1	2.2
Zhepujilieke-13	3827.48	4121.06	0.93	0.274770	0.011437	2.039759	0.120293	0.252342	0.011435	1128.8	40.2	1028.9	10.8
Zhepujilieke-14	1358.56	2114.01	0.64	0.052621	0.001450	0.524326	0.015732	0.072296	0.001228	428.0	4.5	450.0	3.4
Zhepujilieke-15	248.25	560.73	0.44	0.056440	0.002669	0.564608	0.028871	0.072358	0.001783	454.5	8.7	450.3	5.7
Zhepujilieke-16	233.37	494.33	0.47	0.057979	0.006471	0.565142	0.053635	0.072189	0.002829	454.9	4.8	449.3	7.0
Zhepujilieke-17	1197.09	1368.03	0.88	0.052587	0.001847	0.523289	0.019775	0.072457	0.001554	427.3	3.2	450.9	6.3
Zhepujilieke-18	588.81	1770.57	0.33	0.055422	0.002279	0.553013	0.027979	0.072473	0.001871	447.0	4.3	451.0	3.2
Zhepujilieke-19	1538.57	2202.94	0.70	0.052275	0.001889	0.519557	0.020012	0.072538	0.001508	424.9	3.4	451.4	4.1

Table 4. Sr–Nd isotopic compositions of the five studied granites

Sample	$^{87}Rb/^{86}Sr$	$^{87}Sr/^{86}Sr$	2σ	$(^{87}Sr/^{86}Sr)_i$	$^{147}Sm/^{144}Nd$	$^{143}Nd/^{144}Nd$	2σ	$(^{143}Nd/^{144}Nd)_i$	$f_{Sm/Nd}$	εNd(*t*)	T_{DM1}(Ga)	T_{DM2}(Ga)
MDLH-1	1.304	0.720027	4	0.715018	0.1282	0.512383	8	0.512207	−0.34808	−1.4	1.37	1.14
MDLH-2	0.880	0.720014	4	0.716635	0.1305	0.512376	5	0.512197	−0.33644	−1.7	1.42	1.15
MDLH-3	1.080	0.720040	7	0.715890	0.1294	0.512384	4	0.512206	−0.34217	−1.4	1.38	1.14
MDLH-4	0.768	0.720037	8	0.717085	0.1318	0.512388	4	0.512207	−0.33011	−1.5	1.42	1.14
HT-1	3.734	0.745423	9	0.731079	0.1405	0.512389	7	0.512196	−0.28587	−2.5	1.58	1.14
HT-2	2.766	0.733433	8	0.722809	0.1400	0.512394	8	0.512202	−0.28808	−2.4	1.56	1.14
HT-3	3.941	0.745410	8	0.730272	0.1418	0.512381	9	0.512186	−0.27932	−2.7	1.63	1.16
HT-4	3.589	0.733308	5	0.719521	0.1413	0.51239	5	0.512196	−0.28171	−2.5	1.60	1.15
TEG-1	2.565	0.720379	7	0.710527	0.1347	0.512409	7	0.512224	−0.31505	−1.3	1.43	1.12
TEG-2	2.068	0.720389	8	0.712447	0.1322	0.512414	8	0.512232	−0.32789	−1.1	1.37	1.11
TEG-3	2.063	0.720366	5	0.712440	0.1360	0.512403	7	0.512216	−0.30866	−1.5	1.46	1.13
TEG-4	1.960	0.720392	4	0.712865	0.1335	0.51241	4	0.512227	−0.32122	−1.2	1.40	1.12
ZGST-1	1.787	0.715011	5	0.708148	0.1427	0.512322	8	0.512126	−0.27447	−3.2	1.77	1.28
ZGST-2	2.155	0.714998	7	0.706718	0.1432	0.512317	8	0.512120	−0.27179	−3.3	1.80	1.29
ZGST-3	1.400	0.715024	8	0.709646	0.1439	0.512323	5	0.512125	−0.26851	−3.2	1.80	1.28
ZGST-4	1.709	0.715021	7	0.708455	0.1445	0.512325	7	0.512126	−0.26549	−3.2	1.81	1.28
ZPJLK-1	1.244	0.743416	4	0.738636	0.1221	0.51237	4	0.512202	−0.37926	−0.9	1.30	1.14
ZPJLK-2	1.331	0.743426	7	0.738314	0.1342	0.512376	7	0.512192	−0.31784	−1.5	1.48	1.18
ZPJLK-3	0.946	0.743403	8	0.739768	0.1233	0.512364	8	0.512194	−0.37299	−1.1	1.32	1.15
ZPJLK-4	1.098	0.743429	9	0.739210	0.1354	0.512371	9	0.512185	−0.31167	−1.7	1.51	1.19

εNd(*t*) values were calculated using present-day $(^{147}Sm/^{144}Nd)_{CHUR} = 0.1967$ and $(^{143}Nd/^{144}Nd)_{CHUR} = 0.512638$.
T_{DM} values were calculated using present-day $(^{147}Sm/^{144}Nd)_{DM} = 0.2137$ and $(^{143}Nd/^{144}Nd)_{DM} = 0.51315$.

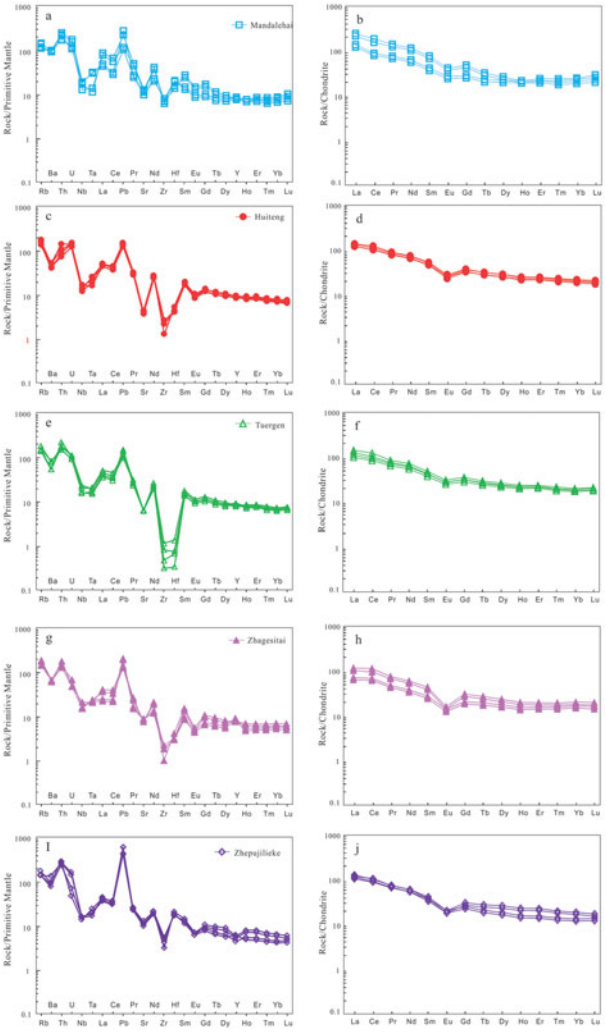

Figure 7. (Colour online) Primitive mantle-nomalized trace element spidergram patterns and chondrite-normalized REE patterns of the studied granites: (a, b) the Mandalehai granites; (c, d) the Huiteng granite; (e, f) the Tuergen granite; (g, h) the Zhagesitai granite; and (i, j) the Zhepujileke granite.

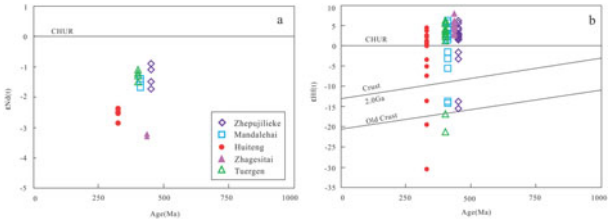

Figure 8. (Colour online) Plot of (a) $\varepsilon_{Nd}(t)$ v. Age (Ma) and (b) $\varepsilon_{Hf}(t)$ v. Age (Ma) for the studied granites from the Chinese Altai.

metaigneous rocks such as orthogneiss, and amphibolite (Miller, 1985; Patiño Douce & Johnston, 1991; Sylvester, 1998). All of the peraluminous granites included in this study are compatible with the 'sediment involvement' trend on the Ba/Th v. $(La/Sm)_N$ plot, indicating a substantial addition of sediments to the source magmas (Fig. 11a). This interpretation is supported by the presence of aluminium-saturated minerals in thin sections, i.e. cordierite, garnet, muscovite and sillimanite (Fig. 3). Previous studies have proposed that the strongly peraluminous felsic rocks in the Chinese Altai were derived from thermal melting of local metasediments (e.g. the Habahe Group), due to heating from the asthenosphere upwelling through a slab window (Cai *et al.* 2011*b*; Yu *et al.* 2016). However, the low zircon saturation temperature (537–765 °C; Fig. 11b) and the existence of residual zircon does not support a high-temperature magmatic event in the Chinese Altai. The metasedimentary rocks of the Habahe Group are overwhelmingly Neoproterozoic to Early Palaeozoic in age, with a prominent detrital zircon age peak around 465–542 Ma (with zircon $\varepsilon_{Hf}(t)$ values of −25 to +15; Jiang *et al.* 2011*b*). Therefore, the oldest zircon xenocrysts in the studied granites, with U–Pb ages from 1294 to 913 Ma and $\varepsilon_{Hf}(t)$

https://doi.org/10.1017/S0016756817001029 Published online by Cambridge University Press

Table 5. Zircon Hf isotopic compositions of the five studied granites

Sample name	$^{176}Hf/^{177}Hf$	1s	$^{176}Yb/^{177}Hf$	1s	$^{176}Lu/^{177}Hf$	1s	$\varepsilon Hf(t)$	T_{DM1}	T_{DM2}
Mandalehai									
MDLH-1	0.282606	0.000014	0.118654	0.005832	0.006320	0.000176	1.51	1065.09	1302.81
MDLH-2	0.282373	0.000019	0.046606	0.001953	0.002117	0.000069	− 5.58	1279.68	1750.06
MDLH-3	0.282144	0.000015	0.066174	0.000586	0.001956	0.000025	− 13.77	1601.31	2258.62
MDLH-4	0.282661	0.000021	0.122804	0.004351	0.004715	0.000139	3.90	928.94	1151.86
MDLH-5	0.282606	0.000017	0.118437	0.000940	0.001018	0.000029	2.97	915.31	1210.79
MDLH-6	0.282486	0.000021	0.097852	0.001865	0.002021	0.000068	− 1.55	1113.65	1496.55
MDLH-7	0.282137	0.000014	0.056682	0.000723	0.001714	0.000008	− 13.95	1600.83	2270.11
MDLH-8	0.282623	0.000025	0.104631	0.002570	0.002785	0.000088	3.09	935.20	1203.44
MDLH-9	0.282681	0.000017	0.035227	0.000757	0.000820	0.000034	5.68	805.32	1039.13
MDLH-10	0.282601	0.000017	0.129265	0.002153	0.002333	0.000071	2.43	955.68	1244.85
MDLH-11	0.282591	0.000023	0.175445	0.002137	0.002316	0.000069	2.09	969.81	1266.94
MDLH-12	0.282734	0.000019	0.108668	0.002215	0.002401	0.000071	7.12	762.73	947.70
MDLH-13	0.282655	0.000020	0.160885	0.001617	0.001752	0.000057	4.51	863.06	1113.73
MDLH-14	0.282437	0.000022	0.081582	0.001584	0.001717	0.000058	− 3.20	1174.53	1600.61
MDLH-15	0.282599	0.000020	0.091553	0.000703	0.000762	0.000026	2.80	918.92	1222.02
Huiteng									
HT-1	0.282603	0.000013	0.117621	0.005361	0.005810	0.000164	− 0.03	1052.28	1333.20
HT-2	0.282370	0.000018	0.046200	0.001796	0.001946	0.000064	− 7.44	1277.04	1800.75
HT-3	0.282598	0.000016	0.128141	0.001979	0.002145	0.000066	0.59	954.09	1294.49
HT-4	0.282025	0.000012	0.047367	0.000399	0.001361	0.000004	− 19.54	1742.80	2558.39
HT-5	0.282588	0.000022	0.173918	0.001965	0.002129	0.000064	0.24	968.19	1316.66
HT-6	0.281713	0.000012	0.043451	0.000547	0.001307	0.000005	− 30.57	2174.66	3243.26
HT-7	0.282620	0.000024	0.103720	0.002363	0.002561	0.000082	1.28	932.76	1250.89
HT-8	0.282678	0.000016	0.034920	0.000696	0.000754	0.000032	3.72	807.14	1096.10
HT-9	0.282434	0.000021	0.080872	0.001456	0.001578	0.000053	− 5.09	1173.43	1653.23
HT-10	0.282596	0.000019	0.090757	0.000646	0.000701	0.000024	0.83	920.65	1279.26
HT-11	0.282658	0.000020	0.121736	0.004000	0.004335	0.000129	2.24	922.20	1189.99
HT-12	0.282193	0.000014	0.054365	0.000562	0.001613	0.000023	− 13.65	1517.30	2190.26
HT-13	0.282652	0.000019	0.159485	0.001487	0.001611	0.000053	2.61	863.06	1166.18
HT-14	0.282603	0.000016	0.117407	0.000864	0.000936	0.000027	1.03	916.54	1266.79
HT-15	0.282483	0.000020	0.097001	0.001715	0.001858	0.000063	− 3.42	1112.03	1547.70
Tuergen									
TEG-1	0.282603	0.000020	0.049234	0.001395	0.001511	0.000049	1.32	931.72	1264.25
TEG-2	0.282625	0.000014	0.041375	0.000715	0.000775	0.000025	2.27	882.84	1204.24
TEG-3	0.282604	0.000017	0.076475	0.001782	0.001932	0.000071	1.26	940.92	1268.13
TEG-4	0.282636	0.000014	0.022988	0.000068	0.000074	0.000003	2.82	851.69	1169.35
TEG-5	0.282059	0.000012	0.059628	0.000632	0.001809	0.000021	− 16.91	1715.61	2448.49
TEG-6	0.282657	0.000015	0.030945	0.000390	0.000422	0.000013	3.48	830.29	1127.33
TEG-7	0.282678	0.000018	0.063424	0.000457	0.000495	0.000003	4.21	802.65	1081.26
TEG-8	0.282628	0.000021	0.086151	0.000916	0.000992	0.000029	2.32	883.70	1200.68
TEG-9	0.282641	0.000022	0.054823	0.000180	0.000195	0.000007	2.97	847.48	1159.91
TEG-10	0.282724	0.000027	0.070754	0.001760	0.001908	0.000054	5.51	766.96	998.60
TEG-11	0.282666	0.000020	0.064829	0.000275	0.000298	0.000015	3.83	815.14	1105.31
TEG-12	0.282727	0.000036	0.069511	0.001035	0.001122	0.000035	5.80	746.65	980.35
TEG-13	0.281932	0.000014	0.052547	0.000579	0.001567	0.000025	− 21.34	1883.13	2724.53
TEG-14	0.282745	0.000034	0.063257	0.001633	0.001769	0.000071	6.28	733.81	949.37
TEG-15	0.282677	0.000041	0.035125	0.000263	0.000285	0.000019	4.22	799.64	1080.43
Zhagesitai									
ZGST-1	0.282651	0.000009	0.071273	0.001184	0.001283	0.000032	4.90	857.08	1102.78
ZGST-2	0.282654	0.000007	0.037349	0.000043	0.000047	0.000002	5.34	826.32	1074.83
ZGST-3	0.282649	0.000012	0.069799	0.000350	0.000380	0.000022	5.08	839.92	1091.27
ZGST-4	0.282594	0.000007	0.031392	0.000049	0.000053	0.000009	3.22	908.66	1209.08
ZGST-5	0.282592	0.000009	0.048602	0.000291	0.000315	0.000006	3.09	916.82	1216.99
ZGST-6	0.282578	0.000009	0.030684	0.000191	0.000206	0.000041	2.63	933.70	1246.66
ZGST-7	0.282686	0.000009	0.046781	0.001015	0.001100	0.000004	6.19	803.26	1020.66
ZGST-8	0.282650	0.000011	0.058227	0.003056	0.003312	0.000002	4.26	908.56	1143.16
ZGST-9	0.282685	0.000007	0.049793	0.000660	0.000715	0.000008	6.24	797.54	1017.53
ZGST-10	0.282680	0.000010	0.049255	0.001043	0.001130	0.000011	5.95	813.41	1036.27
ZGST-11	0.282597	0.000007	0.050628	0.000532	0.000577	0.000027	3.19	916.46	1211.05
ZGST-12	0.282622	0.000007	0.044864	0.000277	0.000300	0.000054	4.14	875.62	1150.53
ZGST-13	0.282685	0.000010	0.065547	0.001838	0.001992	0.000045	5.90	824.13	1038.98
ZGST-14	0.282763	0.000015	0.144635	0.003839	0.004161	0.000014	8.01	757.19	905.43
ZGST-15	0.282629	0.000009	0.060422	0.000401	0.000435	0.000038	4.36	868.74	1136.87
Zhepujilieke									
ZPJLK-1	0.282481	0.000019	0.096157	0.001576	0.001708	0.000058	− 1.61	1110.81	1500.84
ZPJLK-2	0.282618	0.000023	0.102818	0.002172	0.002354	0.000076	3.07	930.82	1205.70
ZPJLK-3	0.282114	0.000012	0.049079	0.000517	0.001507	0.000016	− 13.83	1624.38	2293.63
ZPJLK-4	0.282676	0.000015	0.034616	0.000639	0.000693	0.000030	5.58	809.06	1046.63
ZPJLK-5	0.282596	0.000015	0.127026	0.001819	0.001972	0.000061	2.39	952.92	1248.31
ZPJLK-6	0.282586	0.000021	0.172405	0.001806	0.001957	0.000059	2.04	966.99	1270.45
ZPJLK-7	0.282650	0.000018	0.158097	0.001367	0.001481	0.000049	4.44	863.33	1118.74
ZPJLK-8	0.282703	0.000017	0.104218	0.001733	0.001878	0.000052	6.21	796.12	1006.75
ZPJLK-9	0.282432	0.000020	0.080168	0.001339	0.001451	0.000050	− 3.27	1172.68	1605.71

https://doi.org/10.1017/S0016756817001029 Published online by Cambridge University Press

Table 5. Continued

Sample name	$^{176}Hf/^{177}Hf$	1s	$^{176}Yb/^{177}Hf$	1s	$^{176}Lu/^{177}Hf$	1s	$\varepsilon Hf(t)$	T_{DM1}	T_{DM2}
ZPJLK-10	0.282594	0.000018	0.089967	0.000594	0.000644	0.000022	2.69	922.49	1229.66
ZPJLK-11	0.282601	0.000012	0.116598	0.004929	0.005341	0.000152	1.64	1041.15	1295.72
ZPJLK-12	0.282568	0.000017	0.045798	0.001651	0.001789	0.000059	1.45	988.43	1307.79
ZPJLK-13	0.282066	0.000011	0.052865	0.000487	0.001596	0.000001	− 15.55	1695.97	2401.31
ZPJLK-14	0.282656	0.000019	0.120676	0.003677	0.003985	0.000120	3.96	916.42	1148.99
ZPJLK-15	0.282601	0.000015	0.116385	0.000794	0.000860	0.000025	2.88	917.94	1217.75

The $^{176}Hf/^{177}Hf$ and $^{176}Lu/^{177}Hf$ ratios of chondrite and depleted mantle at present are 0.282772 and 0.0332, 0.28325 and 0.0384; $(^{176}Lu/^{177}Hf)_{LC} = 0.019$; $\lambda = 1.867 \times 10^{-11}$ a^{-1}; t = crystallization time of zircon.
$\varepsilon Hf(t) = \{[(^{176}Hf/^{177}Hf)_S - (^{176}Lu/^{177}Hf)_S \times (e\lambda t - 1)]/[(^{176}Hf/^{177}Hf)_{CHUR} - (^{176}Lu/^{177}Hf)_{CHUR} \times (e\lambda t - 1)] - 1\} \times 10000$.
$T_{DM1} = 1/\lambda \ln\{[(^{176}Hf/^{177}Hf)_S - (^{176}Hf/^{177}Hf)_{DM}]/[(^{176}Lu/^{177}Hf)_S - (^{176}Lu/^{177}Hf)_{DM}] + 1\}$.
$T_{DM2} = t + 1/\lambda \ln\{[(^{176}Hf/^{177}Hf)_S - (^{176}Hf/^{177}Hf)_{DM}]/[(^{176}Lu/^{177}Hf)_{LC} - (^{176}Lu/^{177}Hf)_{DM}] + 1\}$

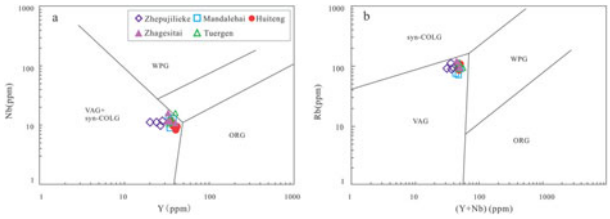

Figure 9. (Colour online) Trace element diagrams for tectonic discrimination: (a) Nb v. Y and (b) Rb v. Y + Nb.

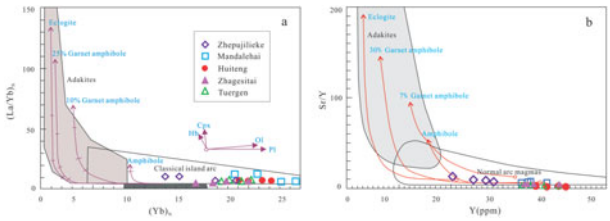

Figure 10. (Colour online) Trace element discrimination diagrams: (a) $(La/Yb)_N$ v. $(Yb)_N$; (b) Sr/Y v. Y.

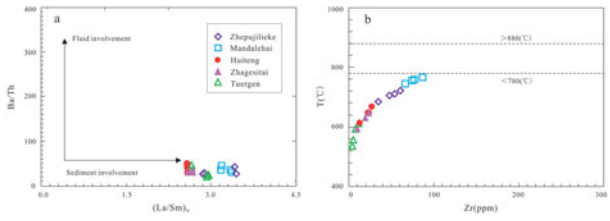

Figure 11. (Colour online) Trace element discrimination diagrams: (a) Ba/Th v. $(La/Sm)_N$; and (b) diagram for variations in zircon saturation temperatures for the studied granites from the Chinese Altai.

values ranging from −30.6 to −13.7 (T_{DM2} = 2190–3243 Ma), are likely to be exotic.

Oceanic sediments mixing into the source magma via dehydration melting are expected to have a composition reflecting their origin as weathering products of upper continental crust (Asahara *et al*. 1999; Bayon *et al*. 2002). The studied granites are characterized by high initial $^{87}Sr/^{86}Sr$ ratios (0.714998–0.743426), negative $\varepsilon_{Nd}(t)$ values (−3.3 to −0.9) and $\varepsilon_{Hf}(t)$ values (−30.6 to −13.7), all of which are typical geochemical characteristics of oceanic sediments (Asahara *et al*. 1999; Bayon *et al*. 2002). Additionally, the Nd/Hf ratios of these granites are both relatively high

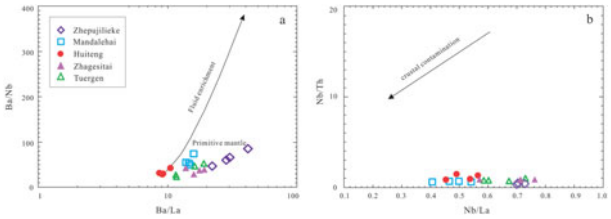

Figure 12. (Colour online) Trace element discrimination diagrams: (a) Ba/Nb v. Ba/La; (b) Nb/Th v. Nb/La.

and quite variable (from 4.26 to 43.57), which is typical of Indian Ocean sediments (Nd/Hf = 6–42, n = 9; Ben Othman, White & Patchett, 1989; Gasparon & Varne, 1998; Plank & Langmuir, 1998). These various lines of evidence support the presence of an oceanic sediment component in the magma sources.

However, the isotopic features of Sr and Nd in whole-rock samples, and Hf in zircons, strongly suggest a heterogeneous source. Previous studies have suggested that mantle-derived components or juvenile crust played an important role in the generation of granites in the CAOB (Sengör, Natal'in & Burtman, 1993; Hu *et al*. 2000; Jahn, Wu & Chen, 2000*b*; Windley *et al*. 2007). The positive zircon $\varepsilon_{Hf}(t)$ values (+0.24 to +8.01), young Hf model ages (905–1317 Ma) and high Mg# values (28.69–53.33) of the studied granites strongly suggest a mantle-derived component. In particular, the characteristics of the zircon Hf isotopic system are consistent with those of other Palaeozoic arc granites from the region ($\varepsilon_{Hf}(t)$ = −1.4 to +12.9, T_{DM2} = 765–2122 Ma, n = 14; Cai *et al*. 2011*b*; Wang *et al*. 2011; Lv *et al*. 2012). Therefore, we proposed that the granites were derived from mixed magmas, incorporating materials from both the partial melting of subducting oceanic sediments and the overlying mantle wedge.

Sr is a more sensitive indicator of fluid introduction than Hf and Nd (Woodhead *et al*. 2001; Münker *et al*. 2004; Turner *et al*. 2009). The initial $^{87}Sr/^{86}Sr$ ratios of the studied granites (0.706718–0.739768) demonstrate a wider range than the initial $^{143}Nd/^{144}Nd$ ratios (0.512120–0.512232), possibly reflecting the addition of fluids into the magma sources (Zhang *et al*. 2016). However, as shown by the plots of Ba/Th v. $(La/Sm)_N$ (Fig. 11a) and Ba/Nb v. Ba/La (Fig. 12a), the

https://doi.org/10.1017/S0016756817001029 Published online by Cambridge University Press

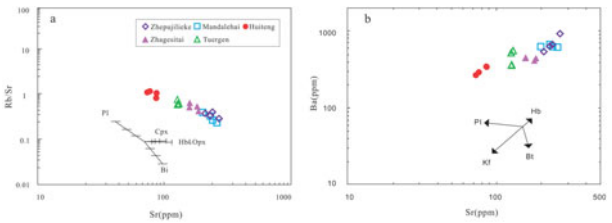

Figure 13. (Colour online) Trace element discrimination diagrams: (a) Rb/Sr v. Sr; (b) Ba v. Sr.

granites are not plotted on the 'fluid involvement' or 'fluid enrichment' lines. This indicates that, although aqueous fluids were important in the generation of initial magma, they did not significantly alter their chemical compositions.

6.2.2. Assimilation of continental crust and fractional crystallization

Previous studies have suggested that correlations between selected major and trace element ratios (such as La/Sm, Nb/La, Th/Ta, Sm/Nd, SiO_2/MgO and Nb/U) can be used to assess the effects of crustal contamination in magmas (Yin *et al*. 2015). No correlation is observed in plots of Sm/Nd v. Nb/La, La/Sm v. Nb/La or Nb/U v. SiO_2/MgO (not shown), ruling out the possibility of significant crustal contamination. On the Nb/Th v. Nb/La plot (Fig. 12b), peraluminous granites plot well away from the 'crustal contamination' trend, indicating that assimilation of the continent crust was minimal. This is further supported by the uniform $\varepsilon_{Nd}(t)$ values and low zircon saturation temperatures (537–765 °C) of the peraluminous granites, which indicate that the magmas did not suffer from assimilation of the surrounding rocks during its intrusion. Therefore, we conclude that the crustal affinities of the peraluminous granites are mainly attributable to melting of oceanic sediments rather than crustal assimilation.

The peraluminous granites show a wider range in MgO contents (0.41–1.40 wt %) and Mg# (28.69–53.33), suggesting that their precursor magmas probably underwent a higher degree of fractional crystallization. The Rb/Sr v. Sr and Ba v. Sr plots (Fig. 13) indicate that fractional crystallization of plagioclase, K-feldspar and biotite played a dominant role in the evolution of the peraluminous magmas.

6.3. Decoupling of Nd and Hf isotopic systems

All samples included in this study showed significant Nd–Hf decoupling (Fig. 8). This signal may have been inherited from the magma source, or may be the result of disequilibrium melting processes (Su *et al*. 2015; Yu *et al*. 2016). Melts may show higher $^{176}Hf/^{177}Hf$ ratios than the source rock if dissolution of zircons is incomplete during partial melting, because the very low Lu/Hf ratio of zircon can result in low, non-radiogenic $^{176}Hf/^{177}Hf$ ratios (e.g. Tang *et al*. 2014; Yu *et al*. 2016). The high Nd/Hf ratios (4.87–37.70) and low Hf concentrations (0.75–3.87 ppm) of the studied granites can be explained by sequestration of Hf in residual zircon, which would lower the concentrations of Hf relative to Nd in melts. Zircon xenocrysts often appear in CL images of the studied granites (Fig. 4), suggesting that the decoupled Nd–Hf isotopic features may be inherited from disequilibrium melting processes.

These results suggest that the studied granites were produced by partial melting of subducting oceanic sediments, as well as the overlying mantle wedge. The old Hf model ages (T_{DM2} = 2190−3243 Ma) and negative $\varepsilon_{Hf}(t)$ values (−30.6 to −13.7) of these xenocrysts suggest a crustal affinity, and a possible derivation from oceanic sediments. Numerous studies have reported significant disequilibrium in the Sr, Nd and Pb isotopic systems during sedimentary or crustal anatexis (e.g. Hogan & Sinha, 1991; Hammouda, 1994; Knesel & Davidson, 1996; Tommasini & Davies, 1997; Davies & Tommasini, 2000). The rate of zircon dissolution is controlled by several factors, including zircon solubility, temperature, zircon crystal size, and the melt and solid phase composition (e.g. Ayres & Harris, 1997; Zeng, Asimow & Saleeby, 2005*a*; Zeng, Saleeby & Asimow, 2005*b*; Farina & Stevens, 2011). A variable rate of zircon dissolution in a single magma source may result in variable Hf isotopic compositions in different batches of melts (Tang *et al*. 2014). Tollstrup & Gill (2005) calculated Zr solubility in a granitic melt using the parameters given by Watson & Harrison (1983), and suggested that for subducted sediments containing 65–165 ppm Zr, temperatures must be lower than 780 °C for any zircon to survive. This finding was supported by Johnson & Plank (1999), who reported sediment melting at 780–825 °C for peraluminous to metaluminous material at 3–4 GPa.

Based on this study, we conclude that zircons from oceanic sediments may have survived in the crystal phase during partial melting, then served as nuclei for recrystallization at the low zircon saturation temperature of the studied granites (Fig. 11b). During the melting process, a significant amount of ^{177}Hf was retained at the source by residual zircons (Tang *et al*. 2014), while the $^{176}Hf/^{177}Hf$ ratio of the melts became correspondingly elevated, and decoupled from the $^{143}Nd/^{144}Nd$ ratio. Residual zircon can explain the wide range of $\varepsilon_{Hf}(t)$ values and Hf model ages seen in these granites, which cannot represent the geochemistry of the primary magma.

In contrast with ^{177}Hf, which can be retained at the source, Nd concentrations cannot be altered by residual zircon during the melting of oceanic sediments. Furthermore, the model ages of the studied granites and their uniform $\varepsilon_{Nd}(t)$ values suggest only minor assimilation of continental crust and fluids during magmatic processes. Consequently, whole-rock Nd isotopic ratios likely represent mixing processes in the parent magmas of the studied granites.

https://doi.org/10.1017/S0016756817001029 Published online by Cambridge University Press

6.4. Implications for the recycling of oceanic sediments

The growth of the Chinese Altai was driven by subduction processes along the margins of the Palaeo-Asian ocean, from the Cambrian (or earlier) through the Devonian (Xiao *et al*. 2004, 2008; Yuan *et al*. 2007; Sun *et al*. 2008, 2009; Cai *et al*. 2010, 2011*a*; Su *et al*. 2011, 2012;). Recent studies have suggested that ridge subduction was probably the dominant tectonic control in the geodynamic evolution of the Chinese Altai. When an actively spreading ocean ridge is dragged into a subduction zone, the oceanic slabs on both sides cease to grow (Dickinson & Snyder, 1979; Thorkelson, 1996; Cai *et al*. 2010; Santosh & Kusky, 2010). High-temperature metamorphism and several types of magmatism will commence, as diverse components of the mantle and downgoing slab are melted by upwelling of hot asthenosphere through the slab window (Geng *et al*. 2009; Zhao *et al*. 2009; Jiang *et al*. 2010; Yin *et al*. 2010; Zhang *et al*. 2010).

However, the low zircon saturation temperature (537–765 °C) of the studied granites does not support the type of high-temperature magmatic event that would be produced by the upwelling of hot asthenosphere in a ridge subduction setting. This is further supported by the appearance of the zircon xenocrysts in CL images (Fig. 4). In addition, Early to Middle Palaeozoic A-type granites and high-temperature metamorphic rocks are scarce in the Chinese Altai (Yuan *et al*. 2007; Sun *et al*. 2008; Cai *et al*. 2011*a*,*b*, 2012, Wang *et al*. 2011; Lv *et al*. 2012), which also suggests 'cold' magmatism during this interval. Experimental studies (Osamu, 1995; Karsten, Klein & Sherman, 1996) have revealed that melts formed in a subduction ridge setting typically develop under low-pressure conditions, whereas the major element composition of the studied granites implies that they formed in a high-pressure environment, most likely a normal subduction zone rather than a ridge subduction setting. Therefore, the ridge subduction model is not supported by the studied granites.

It is generally accepted that subduction is a 'high-pressure' but relatively 'low-temperature' tectonic process, and under most circumstances subducting crustal rocks are too cold to melt. However, recent modelling studies, combined with an improved understanding of the chemistry and petrography of subduction-zone fluids and melts, indicate subduction zones likely meet the conditions for deep slab melt, so long as free fluid is available at sub-arc depths. (Pearce *et al*. 1999; Kempton *et al*. 2002; Nebel *et al*. 2007; Pearce, Kempton & Gill, 2007; Spandler & Pirard, 2013). Subduction zones are sites where chemical components are transferred from the downgoing slab back to the surface (Spandler & Pirard, 2013). Experiments by Grassi & Schmidt (2011) and Hofmann (1997) indicated that subducting slab components can be mechanically or diffusively mix into the ambient mantle, or can return to the continent crust, in the form of chemical components within arc magmas.

Previous studies have proposed that only 15 % of sediment-derived Hf originating in subducting volcanoclastic debris is transported back to the crust via arc magmatism, whereas ~85 % is introduced into the mantle. Since a large amount of Hf can be retained in residual zircons under low-temperature conditions, the proportion of Hf returning to the crust is likely to be lower than 15 %. Therefore, Hf may not be an effective tracer in sediment recycling (Chauvel *et al*. 2009; Handley *et al*. 2011; Zhang *et al*. 2016). In contrast, the concentration and isotopic composition of Nd in arc magmas cannot be altered by residual zircon effects. As a result, Nd may more reliably constrain the relative proportion of recycled oceanic sediment in mixed-source arc magmas. In this study, we have outlined a model to explain how Hf is transferred out of the subducting slab. The significant decoupling between Nd and Hf isotopic compositions in the studied peraluminous granites from the Chinese Altai shows that partial melting of oceanic sediment is a major factor controlling the relationship between the two isotopic systems in island arc environments.

Based on these results, we consider oceanic sediment recycled back into the arc crust was an important component of the source magmas for the studied granites. Approximately 40 % of exposed rocks in the Altai Orogenic Belt are granite, suggesting that over 40 % of continental growth in the orogenic belt is attributable to felsic arc magmatism. This demonstrates that oceanic sediment recycling was an important process in the continental growth of the Chinese Altai, an aspect that has been completely overlooked in previous studies.

7. Conclusions

1. The studied peraluminous granites in the Chinese Altai were emplaced between 449 and 327 Ma. Their parental magmas might be derived from the partial melting of oceanic sediments and the associated mantle wedge in an active subduction zone.

2. A significant amount of ^{177}Hf was retained by residual zircons in the subducting slab, leading to significant decoupling of the Hf and Nd isotopic systems in the peraluminous granites. Whole-rock Nd isotopic ratios can faithfully reflect mixing processes within the parent magma of the peraluminous granites.

3. Oceanic sediment recycling may have played an important role in the crustal growth in the Chinese Altai during the early and middle Palaeozoic.

Acknowledgements. We would like to express our gratitude to Prof. Shengrong Li for his constructive reviews, which significantly improved the manuscript. This work was financially supported by the China University of Petroleum (Beijing) Science Foundation (Project No. 2462014YJRC031), the National Science Foundation of China (Project No. 41502209) and Chinese State Program 973 (Project No. 2015CB250901).

References

Andersen, T. 2002. Correction of common lead in U–Pb analyses that do not report 204Pb. *Chemical Geology* **192**, 59–79.

Anderson, D. L. 1989. *Theory of the Earth*. Oxford: Blackwell, 366 pp.

Anderson, D. L. 2001. Topside tectonics. *Science* **293**, 2016–18.

Anderson, D. L. 2006. Speculations on the nature and cause of mantle heterogeneity. *Tectonophysics* **416**, 7–22.

Asahara, Y., Tanaka, T., Kamioka, H., Nishimura, A. & Yamazaki, T. 1999. Provenance of the north Pacific sediments and process of source material transport as derived from Rb-Sr isotopic systematics. *Chemical Geology* **158**, 271–91.

Ayres, M. & Harris, N. 1997. REE fractionation and Nd-isotope disequilibrium during crustal anatexis: constraints from Himalayan leucogranites. *Chemical Geology* **139**, 249–69.

Bayon, G., German, C. R., Boella, R. M., Milton, J. A., Taylor, R. N. & Nesbitt, R. W. 2002. An improved method for extracting marine sediment fractions and its application to Sr and Nd isotopic analysis. *Chemical Geology* **187**, 179–99.

Ben Othman, D. B., White, W. M. & Patchett, J. 1989. The geochemistry of marine sediments, island arc magma genesis, and crust–mantle recycling. *Earth and Planetary Science Letters* **94**, 1–21.

BGMRX (Bureau of Geology Mineral Resources of Xinjiang Uygur Autonomous Region), 1993. *Regional Geology of Xinjiang Uygur Autonomous Region*. People's Republic of China, Ministry of Geology and Mineral Resources. Geological Memoirs, Series 1, No. 32. Beijing: Geological Publishing Housepp. 6–206 (in Chinese).

Biske, Y. S. & Seltmann, R. 2010. Paleozoic Tianshan as a transitional region between the Rheic and Urals-Turkestan Oceans. *Gondwana Research* **17**, 602–13.

Brenan, J. M., Shaw, H. F., Ryerson, F. J. & Phinney, D. L. 1995. Mineral-aqueous fluid partitioning of trace elements at 900 °C and 2.0 GPa: constraints on the trace element chemistry of mantle and deep crustal fluids. *Geochimica et Cosmochimica Acta* **59**, 3331–50.

Cai, K., Sun, M., Yuan, C., Xiao, W. J., Zhao, G. C., Long, X. P. & Wu, F. Y. 2012. Carboniferous mantle-derived felsic intrusion in the Chinese Altai, NW China: implications for geodynamic change of the accretionary orogenic belt. *Gondwana Research* **22**, 681–98.

Cai, K., Sun, M., Yuan, C., Zhao, G. C., Xiao, W. J., Long, X. P. & Wu, F. Y. 2010. Geochronological and geochemical study of mafic dykes from the northwest Chinese Altai: implications for petrogenesis and tectonic evolution. *Gondwana Research* **18**, 638–52.

Cai, K., Sun, M., Yuan, C., Zhao, G. C., Xiao, W. J., Long, X. P. & Wu, F. Y. 2011a. Geochronology, petrogenesis and tectonic significance of peraluminous granites from the Chinese Altai. *NW China. Lithos* **127**, 261–81.

Cai, K., Sun, M., Yuan, C., Zhao, G., Xiao, W., Long, X. & Wu, F. 2011b. Prolonged magmatism, juvenile nature and tectonic evolution of the Chinese Altai, NW China: evidence from zircon U—Pb and Hf isotopic study of Paleozoic granitoids. *Journal of Asian Earth Sciences* **42**, 949–68.

Chai, F. M., Mao, J. W., Dong, L. H., Yang, F. Q., Liu, F., Geng, X. X. & Zhang, Z. X. 2009. Geochronology of metarhyolites from the Kangbutiebao Formation in the Kelangbasin, Altay Mountains, Xinjiang: implications for the tectonic evolution and metallogeny. *Gondwana Research* **16**, 189–200.

Chauvel, C., Marini, J. C., Plank, T. & Ludden, J. N. 2009. Hf–Nd input flux in the Izu-Mariana subduction zone and recycling of subducted material in the mantle. *Geochemistry, Geophysics, Geosystems* **10**, 514–27.

Chen, B. & Jahn, B. M. 2004.Genesis of post-collisional granitoids and basement nature of the Junggar Terrane, NW China: Nd–Sr isotope and trace element evidence. *Journal of Asian Earth Sciences* **23**, 69–703.

Conrad, C. P. & Lithgow-Bertelloni, C. 2003. How mantle slabs drive plate tectonics. *Science* **298**, 207–9.

Davies, G. R. & Tommasini, S. 2000. Isotopic disequilibrium during rapid crustal anatexis: implications for petrogenetic studies of magmatic processes. *Chemical Geology* **162**, 169–91.

Dickinson, W. R. & Snyder, W. S. 1979. Geometry of subducted slabs related to San Andreas transform. *Journal of Geology* **87**, 609–927.

Farina, F. & Stevens, G. 2011. Source controlled $^{87}Sr/^{86}Sr$ isotope variability in granitic magmas: the inevitable consequence of mineral-scale isotopic disequilibrium in the protolith. *Lithos* **122**, 189–200.

Gasparon, M. & Varne, R. 1998. Crustal assimilation versus subducted sediment input in west Sunda arc volcanics: an evaluation. *Mineralogy & Petrology* **64**, 89–117.

GCRSX (Group for Compilation of Regional Stratigraphy of Xinjiang), 1981. *Regional Stratigraphic Table of NW China: Xinjiang Uygur Autonomous Region Fascicule*. Beijing: Geological Publishing House, pp. 7–11.

Geng, H. Y., Sun, M., Yuan, C., Xiao, W. J., Xian, W. S., Zhao, G. C., Zhang, L. F., Wong, K. & Wu, F. Y. 2009. Geochemical, Sr–Nd and zircon U–Pb–Hf isotopic studies of Late Carboniferous magmatism in the West Junggar, Xinjiang: implications for ridge subduction? *Chemical Geology* **266**, 364–89.

Goolaerts, A., Mattielli, N., Jong, J. D., Weis, D. & Scoates, J. S. 2004. Hf and Lu isotopic reference values for the zircon standard 91500 by MC-ICP-MS. *Chemical Geology* **206**(1–2), 1–9.

Grassi, D. & Schmidt, M. W. 2011. The melting of carbonated pelites from 70 to 700 km depth. *Journal of Petrology* **52**, 765–89.

Hammouda, B. 1994. Random phase approximation for compressible polymer blends. *Journal of Non-Crystalline Solids* **172–174**, 927–31.

Han, B. F., Wang, S. G., Jahn, B. M., Hong, D. W., Kagami, H. & Dun, Y. L. 1997. Depleted-mantle source for the Ulungur River A-type granites from North Xinjiang, China: geochemistry and Nd-Sr isotopic evidence, and implications for Phanerozoic crustal growth. *Chemical Geology* **138**, 135–59.

Handley, H. K., Turner, S., Macpherson, C. G., Gertisser, R. & Davidson, J. P. 2011. Hf-Nd isotope and trace element constraints on subduction inputs at island arcs: limitations of Hf anomalies as sediment input indicators. *Earth and Planetary Science Letters* **304**, 212–23.

He, Z. Y., Sun, L. X., Mao, L. J., Zong, K. Q. & Zhang, Z. M. 2015. Zircon U–Pb and Hf isotopic study of gneiss and granodiorite from the southern Beishan orogenic collage: Mesoproterozoic magmatism and crustal growth. *Chinese Science Bulletin* **60**, 389–99 (in Chinese with English abstract).

https://doi.org/10.1017/S0016756817001029 Published online by Cambridge University Press

Hofmann, A. W. 1997. Mantle geochemistry: the message from oceanic volcanism. *Nature* **385**, 219–29.

Hogan, J. P. & Sinha, A. K. 1991.The effect of accessory minerals on the redistribution of lead isotopes during crustal anatexis: a model. *Geochimica et Cosmochimica Acta* **55**, 335–48.

Hong, D., Zhang, J., Wang, T., Wang, S. & Xie, X. 2004. Continental crustal growth and the super continental cycle: evidence from the Central Asian Orogenic Belt. *Journal ofAsian Earth Sciences* **23**, 799–813.

Hu, A. Q., Jahn, B. M., Zhang, G. X., Chen, Y. B. & Zhang, Q. F. 2000. Crustal evolution and Phanerozoic crustal growth in northern Xinjiang: Nd isotopic evidence. Part I. Isotopic characterization of basement rocks. *Tectonophysics* **328**, 15–51.

Iizuka, T. & Hirata, T. 2005. Improvements of precision and accuracy in in-situ Hf isotope microanalysis of zircon using the laser ablation-MC–ICPMS technique. *Chemical Geology* **220**, 121–37.

Jahn, B. M. & Condie, K. C. 1995.Evolution of the Kaapvaal Craton as viewed from geochemical and SmNd isotopic analyses of intracratonic pelites. *Geochimica et Cosmochimica Acta* **59**(11), 2239–58.

Jahn, B. M., Windley, B. F., Natalin's, B. & Dobretsov, N. 2004. Phanerozoic continental growth in central Asia. *Journal of Asian Earth Sciences* **23**, 599–603.

Jahn, B. M., Wu, F. Y. & Chen, B. 2000a. Granitoids of the Central Asian Orogenic Belt and continental growth in the Phanerozoic. *Transactions of the Royal Society of Edinburgh: Earth Sciences* **91**, 181–93.

Jahn, B. M., Wu, F. & Chen, B. 2000b. Granitoids of the Central Asian orogenic belt and continental growth in the Phanerozoic. *Transaction of Royal Society of Edinburgh Earth Science* **91**, 181–93.

Jarrard, R. D. 1986. Relations among subduction parameters. *Reviews of Geophysics* **24**, 217–84.

Jiang, Y. D., Sun, M., Zhao, G. C., Yuan, C., Xiao, W. J., Xia, X. P., Long, X. P. & Wu, F. Y. 2011. Precambrian detrital zircons in the Early Paleozoic Chinese Altai: their provenance and implications for the crustal growth of central Asia. *Precambrian Research* **189**, 140–54.

Jiang, Y. D., Sun, M., Zhao, G. C., Yuan, C., Xiao, W. J., Xia, X. P., Long, X. P. & Wu, F. Y. 2010. The 390 Ma high-T metamorphism in the Chinese Altai: consequence of ridge-subduction? *American Journal of Science* **310**(10), 1421–52.

Johnson, M. C. & Plank, T. 1999. Dehydration and melting experiments constrain the fate of subducted sediments. *Geochemistry, Geophysics, Geosystems* **1**, 1007. doi: 10.1029/1999GC000014.

Karsten, J. L., Klein, E. M. & Sherman, S. B. 1996. Subduction zone geochemical characteristics in ocean ridge basalts from the southern Chile Ridge: implication of modern ridge subduction systems for the Archean. *Lithos* **37**, 143–61.

Kempton, P. D., Pearce, J. A., Barry, T. L., Fitton, J. G., Langmuir, C. & Christie, D. M. 2002. Sr–Nd–Pb–Hf isotope results from ODP leg 187: evidence for mantle dynamics of the Australian–Antarctic Discordance and origin of the Indian MORB source. *Geochemistry Geophysics Geosystems* **3**, 1–35.

Kessel, R., Schmidt, M. W., Ulmer, P. & Pettke, T. 2005. Trace element signature of subduction-zone fluids, melts and supercritical liquids at 120–180 km depth. *Nature* **437**, 724–7.

Knesel, K. M. & Davidson, J. P. 1996. Isotopic disequilibrium during melting of granite and implications for crustal contamination of magmas. *Geology* **24**, 243–6.

Kröner, A., Hegner, E., Lehmann, B., Heinhorst, J., Wingate, M., Liu, D. & Ermelov, P. 2008.Palaeozoic arc magmatism in the Central Asian Orogenic Belt of Kazakhstan: SHRIMP zircon ages and whole-rock Nd isotopic systematics. *Journal of Asian Earth Sciences* **32**, 118–30.

Kröner, A., Kovach, V., Belousova, E., Hegner, E., Armstrong, R., Dolgopolova, A., Seltmann, R., Alexeiev, D. V., Hoffmann, J. E., Wong, J., Sun, M., Cai, K., Wang, T., Tong, Y., Wilde, S. A., Degtyarev, K. E. & Rytsk, E. 2014. Reassessment of continental growth during the accretionary history of the Central Asian Orogenic Belt. *Gondwana Research* **25**, 103–25.

Long, X. P., Sun, M., Yuan, C., Xiao, W. J., Lin, S. F., Wu, F. Y., Xia, X. P. & Cai, K. D. 2007. U–Pb and Hf isotopic study of zircons from metasedimentary rocks in the Chinese Altai: implications for Early Palaeozoic tectonic evolution. *Tectonics* **26**, TC5015. doi: 10.1029/2007TC002128.

Long, X. P., Yuan, C., Sun, M., Xiao, W., Wang, Y., Cai, K. & Jiang, Y. 2012. Geochemistry and Nd isotopic composition of the Early Paleozoic flysch sequence in the Chinese Altai, Central Asia: evidence for a northward-derived mafic source and insight into Nd model ages in accretionary orogen. *Gondwana Research* **22**, 554–66.

Long, X. P., Yuan, C., Sun, M., Xiao, W. J., Zhao, G. C., Wang, Y. J. & Cai, K. D. 2010. Detrital zircon ages and Hf isotopes of the early Paleozoic Flysch sequence in the Chinese Altai, NW China: new constraints on depositional age, provenance and tectonic evolution. *Tectonophysics* **180**, 213–31.

Lv, Z. H., Zhang, H., Tang, Y. & Guan, S. J. 2012. Petrogenesis and magmatic hydrothermal evolution time limitation of Kelumute No. 112 pegmatite in Altay, Northwestern China: evidence from zircon U—Pb and Hf isotopes. *Lithos* **154**, 374–91.

McCulloch, M. T. & Gamble, J. 1991. Geochemical and geodynamical constraints on subduction zone magmatism. *Earth and Planetary Science Letters* **102**, 358–74.

Miller, C. F. 1985. Are strongly peralumious magmas derived from pelitic-sedimentary sources? *J. Geol.* **93**, 673–89.

Münker, C., Worner, G., Yogodzinski, G. & Churikova, T. 2004. Behaviour of high field strength elements in subduction zones: constraints from Kamchatka-Aleutian arc lavas. *Earth and Planetary Science Letters* **224**, 275–93.

Nebel, O., Münker, C., Nebel-Jacobsen, Y. J., Kleine, T., Mezger, K. & Mortimer, N. 2007. Hf-Nd-Pb isotope evidence from Permian arc rocks for the long-term presence of the Indian-Pacific mantle boundary in the SW Pacific. *Earth and Planetary Science Letters* **254**, 377–92.

Osamu, K. 1995. Migration of igneous activities related to ridge subduction in Southwest Japan and the East Asian continental margin from the Mesozoic to the Paleogene. *Tectonophysics* **245**, 25–35.

Patiño Douce, A. E. & Johnston, A. D. 1991. Phase equilibria and melt productivity in the pelitic system: implications for the origin of peraluminous granitoids and aluminous granulites. *Contributions to Mineralogy and Petrology* **107**, 202–18.

Pearce, J. A., Kempton, P. D. & Gill, J. B. 2007. Hf–Nd evidence for the origin and distribution of mantle domains in the SW Pacific. *Earth and Planetary Science Letters* **260**, 98–114.

Pearce, J. A., Kempton, P. D., Nowell, G. M. & Noble, S. R. 1999. Hf-Nd element isotope perspective on the nature and provenance of mantle and subduction components in Western Pacific arc-basin systems. *Journal of Petroleum Geology* **40**, 1579–611.

Pearce, J. A. & Peate, D. W. 1995. Tectonic implications of the compositions of volcanic arc magmas. *Annual Review of Earth and Planetary Sciences* **23**, 251–85.

Plank, T. & Langmuir, C. H. 1998. The chemical composition of subducting sediment and its consequences for the crust and mantle. *Chemical Geology* **145**, 325–94.

Safonova, I. Y., Buslov, M. M., Iwata, K. & Kokh, D. A. 2004. Fragments of Vendian-Early Carboniferous oceanic crust of the Paleo-Asian Ocean in foldbelts of the Altai Sayan region of Central Asia: geochemistry, biostratigraphy and structural setting. *Gondwana Research* **7**, 771–90.

Santosh, M. & Kusky, T. 2010. Origin of paired high pressure-ultrahigh-temperature orogens: a ridge subduction and slab window model. *Terra Nova* **22**, 35–42.

Sengör, A. M. C. & Natal'in, B. A. 1996. Turkic-type orogeny and its role in the making of the continental crust. *Annual Review of Earth and Planetary Sciences* **24**, 263–337.

Sengör, A. M. C., Natal'in, B. A. & Burtman, V. S. 1993. Evolution of the Altaid tectonic collage and Paleozoic crustal growth in Eurasia. *Nature* **364**, 299–307.

Spandler, C. & Pirard, C. 2013. Element recycling from subducting slabs to arc crust: a review. *Lithos* **170–171**, 208–23.

Staudigel, H., Davies, G. R., Hart, S. R., Marchant, K. M. & Smith, B. M. 1995. Large scale isotopic Sr, Nd and O isotopic anatomy of altered oceanic crust: DSDP/ODP sites 417/418. *Earth and Planetary Science Letters* **130**(1–4), 169–85.

Su, B. X., Qin, K. Z., Lu, Y. H., Sun, H. & Sakyi, P. A. 2015. Decoupling of whole-rock Nd-Hf and zircon Hf-O isotopic compositions of a 284 Ma mafic-ultramafic intrusion in the Beishan Terrane, NW China. *International Journal of Earth Sciences* **104**, 1721–37.

Su, B. X., Qin, K. Z., Sakyi, P. A., Li, X. H., Yang, Y. H., Sun, H., Tang, D. M., Liu, P. P., Xiao, Q. H., Malaviarachchi, S. P. K. 2011. U—Pb ages and Hf-O isotopes of zircons from Late Paleozoic mafic-ultramafic units in southern Central Asian Orogenic Belt: tectonic implications and evidence for an Early-Permian mantle plume. *Gondwana Research* **20**, 516–31.

Sun, M., Long, X. P., Cai, K. D., Jiang, Y. D., B. Y, W., Yuan, C., Zhao, G. C., Xiao, W. J. & Wu, F. Y. 2009. Early Paleozoic ridge subduction in the Chinese Altai: insight from the abrupt change in zircon Hf isotopic compositions. *Science in China* **39**, 1–14.

Sun, M., Yuan, C., Xiao, W., Long, X., Xia, X., Zhao, G., Lin, S., Wu, F. & Kröner, A. 2008. Zircon U—Pb and Hf isotopic study of gneissic rocks from the Chinese Altai: progressive accretionary history in the early to middle Palaeozoic. *Chemical Geology* **247**, 352–83.

Sylvester, P. J. 1998. Post-collisional strongly peraluminous granites. *Lithos* **45**, 29–44.

Tang, M., Wang, X. L., Shu, X. J., Wang, D., Yang, T. & Gopon, P. 2014. Hafnium isotopic heterogeneity in zircons from granitic rocks: geochemical evaluation and modeling of 'zircon effect' in crustal anatexis. *Earth and Planetary Science Letters* **389**, 188–99.

Tatsumi, Y. 1989. Migration of fluid phases and genesis of basalt magmas in subduction zones. *Journal of Geophysical Research* **94**, 4697–707.

Thorkelson, D. J. 1996. Subduction of diverging plates and the principles of slab window formation. *Tectonophysics* **255**, 47–63.

Tollstrup, D. L. & Gill, J. B. 2005. Hafnium systematics of the Mariana arc: evidence for sediment melt and residual phases. *Geology* **33**, 737–40.

Tommasini, S. & Davies, G. R. 1997. Isotope disequilibrium during anatexis: a case study of contact melting, Sierra Nevada, California. *Earth and Planetary Science Letters* **148**, 273–85.

Tong, Y., Wang, T., Hong, D. W., Dai, Y. J., Han, B. F. & Liu, X. M. 2007. Ages and origin of the early Devonian granites from the north part of Chinese Altai Mountains and its tectonic implications. *Acta Petrologica Sinica* **23**, 1933–44.

Turcotte, D. L. & Schubert, G. 2002. *Geodynamics*. Cambridge, Cambridge University Press, 456 pp.

Turner, S., Handler, M., Bindeman, I. & Suzuki, K. 2009. New insights into the origin of O-Hf-Os isotope signatures in arc lavas from Tonga-Kermadec. *Chemical Geology* **266**, 196–202.

Wang, T., Hong, D. W., Jahn, B. M., Tong, Y., Wang, Y. B., Han, B. F. & Wang, X. X. 2006. Timing, petrogenesis, and setting of Paleozoic synorogenic intrusions from the Altai Mountains, northwest China: implications for the tectonic evolution of an accretionary Orogen. *Journal of Geology* **114**, 735–51.

Wang, T., Jahn, B. M., Kovach, V. P., Tong, Y., Hong, D. W. & Han, B. F. 2009. Nd-Sr isotopic mapping of the Chinese Altai and implications for continental growth in the Central Asian Orogenic Belt. *Lithos* **110**, 359–72.

Wang, Y. J., Long, X., Wilde, S., Xu, H., Sun, M., Xiao, W., Yuan, C. & Cai, K. 2014. Provenance of Early Paleozoic metasediments in the central Chinese Altai: implications for tectonic affinity of the Altai-Mongolia terrane in the Central Asian Orogenic Belt. *Lithos* **210–211**, 57–68.

Wang, Y. J., Yuan, C., Long, X. P., Sun, M., Xiao, W. J., Zhao, G. C., Cai, K. D. & Jiang, Y. D. 2011. Geochemistry, zircon U—Pb ages and Hf isotopes of the Paleozoic volcanic rocks in the northwestern Chinese Altai: petrogenesis and tectonic implications. *Journal of Asian Earth Sciences* **42**, 969–85.

Watson, E. B. & Harrison, T. M. 1983. Zircon saturation revisited: temperature and composition effects in a variety of crustal magma types. *Earth and Planetary Science Letters* **64**(2), 295–304.

White, W. M. & Patchett, J. 1984. Hf Nd Sr isotopes and incompatible element abundances in island arcs: implications for magma origins and crust-mantle evolution. *Earth and Planetary Science Letters* **67**(2), 167–85.

Windley, B. F., Alexeiev, D., Xiao, W., Kroner, A. & Badarch, G. 2007. Tectonic models for accretion of the Central Asian Orogenic Belt. *Journal of the Geological Society* **164**, 31–47.

Windley, B. F., Kröner, A., Guo, J., Qu, G., Li, Y. & Zhang, C. 2002. Neoproterozoic to Palaeozoic geology of the Altai orogen, NW China: new zircon age data and tectonic evolution. *Journal of Geology* **110**, 719–39.

Woodhead, J. D., Hergt, J. M., Davidson, J. P. & Eggins, S. M. 2001. Hafnium isotope evidence for 'conservative' element mobility during subduction processes. *Earth and Plane Science Letters* **192**, 331–46.

Xiao, W. J., Han, C. M., Yuan, C., Sun, M., Lin, S. F., Chen, H. L., Li, Z. L., Li, J. L. & Sun, S. 2008. Middle Cambrian to Permian subduction-related accretionary orogenesis of Northern Xinjiang, NW China: implications for the tectonic evolution of central Asia. *Journal of Asian Earth Sciences* **32**, 102–17.

Xiao, W. J., Huang, B. C., Han, C. M., Sun, S. & Li, J. L. 2010. A review of the western part of the Altaids: a key to understanding the architecture of accretionary orogens. *Gondwana Research* **18**, 253–73.

Xiao, W. J., Kröner, A. & Windley, B. 2009. Geodynamic evolution of Central Asia in the Paleozoic and Mesozoic. *International Journal of Earth Sciences* **98**, 1185–8.

Xiao, W. J. & Santosh, M. 2014. The western Central Asian Orogenic Belt: a window to accretionary orogenesis and continental growth. *Gondwana Research* **25**(4), 1429–44.

Xiao, W. J., Windley, B. F., Badararch, G., Li, J., Sun, S., Qin, K. & Wang, Z. 2004. Palaeozoic accretionary and convergent tectonics of the southern Altaids: implications for the growth of central Asia. *Journal of Geological Society London* **161**, 1–4.

Xiao, Y., Zhang, H. F., Shi, J. A., Su, B. X., Sakyi, P. A., Hu, Y. & Zhang, Z. 2011. Late Paleozoic magmatic record of East Junggar, NW China and its significance: implication from zircon U—Pb dating and Hf isotope. *Gondwana Research* **20**, 532–42.

Xie, L. W., Zhang, Y. B., Zhang, H. H., Sun, J. F. & Wu, F. Y. 2008. In situ simultaneous determination of trace elements, U-Pb and Lu-Hf isotopes in zircon and baddeleyite. *Science in China Series D: Earth Sciences* **53**, 220–8.

Yakubchuk, A. S. 2004. Architecture and mineral deposit settings of Altaid orogenic collage: a revised model. *Journal of Asian Earth Sciences* **23**, 761–79.

Yang, J. H., Wu, F. Y., Wilde, S. A., Xie, L. W., Yang, Y. H. & Liu, X. M. 2007. Tracing magma mixing in granite genesis: in situ U—Pb dating and Hf isotope analysis of zircons. *Contributions to Mineralogy and Petrology* **153**, 177–90.

Yin, J. Y., Chen, W., Yuan, C., Yu, S., Xiao, W. J., Long, X. P., Li, J. & Sun, J. B. 2015. Petrogenesis of Early Carboniferous adakitic dikes, Sawur region, northern West Junggar, NW China: implications for geodynamic evolution. *Gondwana Research* **27**, 1630–45.

Yin, J. Y., Yuan, C., Sun, M., Long, X. P., Zhao, G. C. & Geng, H. Y. 2010. Late Carboniferous High-Mg dioritic dykes in Western Junggar, NW China: geochemical features, petrogenesis and tectonic implications. *Gondwana Research* **17**, 145–52.

You, C. F., Castillo, P. R., Gieskes, J. M., Chan, L. H. & Spivack, A. J. 1996. Trace element behaviour in hydrothermal experiments: implications for fluid processes at shallow depths in subduction zones. *Earth and Planetary Science Letters* **140**, 41–52.

Yu, Y., Sun, M., Long, X. P., Li, P. F., Zhao, G. C., Kröner, A., Broussolle, A. & Yang, J. H. 2016. Whole-rock Nd-Hf isotopic study of I-type and peraluminous granitic rocks from the Chinese Altai: constraints on the nature of the lower crust and tectonic setting. *Gondwana Research* **47**, 142–60.

Yuan, H., Gao, S., Liu, X., Li, H., Günther, D. & Wu, F. 2004. Accurate U—Pb age and trace element determinations of zircon by laser ablation-inductively coupled plasma mass spectrometry. *Geostandards and Geoanalytical Research* **28**, 353–70.

Yuan, C., Sun, M., Xiao, W. J., Li, X. H., Chen, H. L., Lin, S. F., Xia, X. P. & Long, X. P. 2007. Accretionary orogenesis of the Chinese Altai: insights from Paleozoic granitoids. *Chemical Geology* **242**, 22–39.

Zeng, L.-S., Asimow, P. D. & Saleeby, J. B. 2005a. Coupling of anatectic reactions and dissolution of accessory phases and the Sr and Nd isotope systematics of anatectic melts from a metasedimentory source. *Geochimica et Cosmochimica Acta* **69**, 3671–82.

Zeng, L.-S., Saleeby, J. B. & Asimow, P. 2005*b*. Nd isotopic disequilibrium during crustal anatexis: a record from the Goat Ranch migmatite complex, southern Sierra Nevada batholith, California. *Geology* **33**, 53–6.

Zhang, C., Liu, L. F., Santosh, M. & Zhang, X. 2016. Sediment recycling and crustal growth in the Central Asian Orogenic Belt: evidence from Sr-Nd-Hf isotopes and trace elements in granitoids of the Chinese Altay. *Gondwana Research* **47**, 142–60.

Zhang, H. F., Sun, M., Lu, F. X., Zhou, X. H., Zhou, M. F., Liu, Y. S. & Zhang, G. H. 2001. Geochemical significance of a garnet lherzolite from the Dahongshan kimberlite, Yangtze Craton, southern China. *Geochemical Journal* **35**, 315–31.

Zhang, Z. M., Zhao, G. C., Santosh, M., Wang, J. L., Dong, X. & Shen, K. 2010. Late Cretaceous charnockite with adakitic affinities from the Gangdese batholith, southeasternTibet: evidence for Neo-Tethyan mid-ocean ridge subduction? *Gondwana Research* **17**, 615–31.

Zhao, Z. H., Xiong, X. L., Wang, Q., Bai, Z. H. & Qiao, Y. L. 2009. Late Paleozoic underplating in North Xinjiang: evidence from shoshonites and adakites. *Gondwana Research* **16**, 216–26.